ECOLE POLYTECHNIQUE - PROMOTION X2007

Alexandre NICOLAS

RESEARCH INTERNSHIP REPORT

Instabilities in the Shear-Banded Flow of Giant Worm-like Micelles

under the supervision of **Dr. Alexander MOROZOV**

- NON CONFIDENTIAL -

Option: Physique

Champ de l'option: Matière molle, fluides complexes, bio-mécanique et MEMS (MEC593)

Directeur de l'option: Prof. David QUÉRÉ

Directeur de stage: Dr. Alexander MOROZOV

Dates du stages: du 8 avril au 13 août 2010

Adresse de l'organisme: *School of Physics & Astronomy, University of Edinburgh , JCMB, King's Buildings, Mayfield road, Edinburgh EH9 3JZ*

Abstract

Many worm-like micellar solutions display dramatic shear-thinning behaviour, which results from the disentanglement of worm-like micelles under shear. This can lead to a stress plateau in the flow curve, corresponding to a shear-banded state in which a viscous low-shear band coexists with a much less viscous band. Recent experimental observations in Taylor-Couette geometry [4, 14] have shown that the purely azimuthal shear-banded flow is not stable. After a selective overview of the rheology of worm-like micelles and a presentation of the theory of shear-banding, we simulate numerically the base shear-banded flow using a Johnson-Segalman constitutive model with parameters fitted to experimental data (collected by S. Lerouge). A linear stability analysis in 3D is then performed, for the first time in Taylor-Couette geometry, to our knowledge. The flow is found to be unstable and we show that this instability is of the viscoelastic type at large Weissenberg numbers. The instability has a different origin close to the onset of the plateau, . We demonstrate the occurrence of a change of most unstable eigenmodes. Finally, we propose alternative approaches for the study of the shear-banded flow.

Résumé

De nombreuses solutions de micelles géantes, ou ver-micelles, se caractérisent par un comportement rhéo-fluidifiant spectaculaire. Cela conduit dans certains cas à un plateau de contrainte sur la courbe constitutive du fluide, lequel correspond à une situation de coexistence de deux bandes de cisaillement: l'une, peu visqueuse et fortement cisaillée, l'autre, visqueuse et peu cisaillée. Des expériences récentes [4, 14] menées dans des cellules de Couette-Taylor font état de l'instabilité de l'écoulement en bandes de base, à savoir purement orthoradial. Après un bref panorma de certains aspects de la rhéologie des ver-micelles et un rappel de la théorie sous-jacente à l'écoulement en bandes de cisaillement, nous décrivons nos simulations numériques du système non-perturbé, obtenu à l'aide du modèle constitutif de Johnson-Segalman paramétré en tenant compte de données expérimentales (recueillies par S. Lerouge). Une analyse de stabilité linéaire en 3 dimensions est ensuite effectuée, ce qui - pour autant que nous le sachions - est une première en géométrie cylindrique. Nos résultats indiquent que l'écoulement est instable et nous montrons que cette instabilité est de type viscoélastique à grand nombre de Weissenberg. Au début du plateau de contraintes, en revanche, l'instabilité a une origine différente. Nous mettons en évidence le changement de mode le plus instable. Enfin, nous proposons des solutions alternatives pour l'étude de l'écoulement en bandes de cisaillement.

Contents

Introduction

Hydre absolue, ivre de ta chair bleue,
Qui te remords l'étincelante queue,
Dans un tumulte au silence pareil.
P. Valéry, Le cimetière marin

Strange though their name might be, worm-like micellar solutions are not products exclusively synthesized for laboratory experiments: a typical example of such a solution that is used in everyday life is shampoo. At first sight, it is puzzling that this fluid, which is basically a mixture of water and soap, should be so viscous. In fact, what accounts for the large viscosity is the aggregation of the so-called surfactant molecules that soap is made of, into very long tubes, up to 100 or 1000 times longer than they are wide; now then, those tubes are strongly entangled at reasonably high surfactant concentration, hence the viscosity. The tubular aggregates are said to be worm-like because they are semi-flexible and, in consequence, winding.

As pointed out by Cates [7], if micellar solutions were as viscous as they are in the limit of zero-shear, the shampoo bottle would be likely to break before one manages to squeeze shampoo out of it. In effect, micellar solutions can display dramatic shear-thinning behaviour, that is, their apparent viscosity can decrease as the shear rate increases. In a number of systems, for some range of applied shear-rates, this results in the coexistence of two physically distinct phases, a viscous one with low shear rate and a highly-sheared one. Since those phases are usually structured in bands, this singular phenomenon is called shear-banding.

Recent experimental observations [4, 14] in a Taylor-Couette rheometer, ie between two concentric cylinders, have shown that the purely azimuthal shear-banded flow is unstable and perturbations set in. So far, to the best of our knowledge, only 2D-simulations had been undertaken in this geometry. The central theme of my internship and, subsequently, of this report is therefore the numerical study of the Taylor-Couette shear-banded flow and its three-dimensional linear stability analysis using a given constitutive model, namely the Johnson-Segalman model. Athough worm-like micelles do have numerous applications in cosmetics or, like polymers, drag reduction in hydrodynamic flows of Newtonian fluids, the present work - let us not be afraid to state this clearly - has no immediate industrial applications (that we can think of, at least). However, giant micelles have come to be model systems in certain fields in rheology, notably because their aggregation process is dynamic

and spares them from irreversible degradation under shear; they have thus been widely studied, but much about them still remains either unexplained or not satisfactorily explained.

The first section of this report is a concise introductory chapter to the physics of worm-like micelles, from their aggregation process to a very partial view of their linear rheology. This chapter owes its presence here to at least two factors: first, getting an overview of the microscopic processes at work in micellar solutions will help us understand how well founded macroscopic models are and possibly better interpret some of our results; then, beautiful physics is involved in it. The second chapter deals with the theory of shear-banding and our numerical approach to it. Then we shall look for instabilities in the next chapter and propose an interpretation concerning their nature in the following one. Those last three chapters are actually a detailed version of an article we have written (A.N. Morozov & A. Nicolas, to be published). Chapter V presents alternative approaches to the study of the shear-banded system, one of which is still ongoing work. Finally, Chapter VI sheds light on some concerns about experimental measurements that we came into in the course of the internship, and it quickly relates a short-lived experimental attempt.

Chapter 1

Introduction to the physics of worm-like micelles

This introductory section offers a very brief overview of the chemical nature, the microscopic organisation and the basic linear rheology of giant worm-like micelles. Since this part has not been the focus of my internship, I am fully indebted to the works and reviews of Cates [7], Lerouge [2], Cappelaere [11], Larson [10], Rehage & Hoffmann [6], Berret [5], Quéré [8], Israelashvili [9] for its content.

1.1 Physical Chemistry of giant worm-like micelles

1.1.1 General features and chemical composition

Famous light scattering experiments undertaken by Debye and Anacker ([1]) in the 1950s have shown that the addition of a salt to a micellar solution results in an increasing intensity ratio between two distinct scattering angles, hence, growing anisotropy of the the aggregates in the solution. From this they concluded that the addition of salt induces an increase in size of the micelles.

More basically, this result implies that micelles are not static, unbreakable molecules brought together by covalent bonds, but, instead, dynamics aggregates resulting from the self-assembly of molecular bricks. Due to their ability to increase in size or, as we shall see later, break and recombine, they are also called *living polymers*, in contrast with their unbreakable (as far as only thermal motion is involved), static counterparts. Their altenatve name, *giant worm-like micelles*, comes from their length ("*giant*"), which can reach a few hundred nanometers [6] or even a few microns, to be compared with their nanometric radius. Their contour length is also much larger than their persistence length (typical values are around 20nm [10] or 40nm [5], slightly below the persistence length of double-chain DNA), thereby making them semiflexible, hence "*worm-like*".

The molecular bricks micelles are made of are surfactants[1]. Their unusual aggregation properties stem from their being amphiphiles, which means that they are composed of a hydrophilic head group and a lipophilic tail. The head group is often ionic, whereas the tail is most of the time a hydrocarbon. Surfactants can occasionnally have several tails; classical two-tail examples are biological lipids.

1.1.2 Examples

Giant worm-like micelles, albeit model systems for rheologic studies [5], are not confined to laboratory rheometers, but can be found in common substances in everyday life. For instance, shampoo consists of surfactant molecules which provide both its detergent capactity and its viscous texture. Indeed, bearing in mind that shampoo is mostly a mixture of water and soap, one might be arrested by the fact that it does not flow through our fingers when poured on their hands if the highly entangled worm-like aggregates built up by the surfactants it contains are not taken into account. Those surfactants are mostly the (omnipresent in cosmetics) sodium laureth sulfate ($CH_3(CH_2)_{10}CH_2(OCH_2CH_2)_nOSO_3Na$) and cetrimonium chloride ($C_{19}H_{42}NCl$). They are also major constituents in most cosmetics, insofar as they are responsible for their gel-like structure. Viscoelastic surfactants are also used in slightly less common complex fluids, such as drilling fluids for oil-recovery [7]. Though not necessarily in their giant worm-like form, they can also be added to hydrodynamic flows in order to reduce drag in Newtonian turbulence.

In rheology, some molecules closely related to the two aforementioned surfactants are broadly used: sodium lauryl sulfate, also known as SDS ($C_{12}H_{25}SO_4Na$), and, above all, hexadecyltrimethylammonium bromide, more commonly named CTAB ($C_{19}H_{42}BrN$), more expensive than its counterpart used in shampoos but exhibiting good agreement with the standard behaviour predicted by theory.

Not surprisingly, the specific nature of the surfactant impacts the values of the persistence length and the contour length of the micelles, as well as optical properties of the solution [6]. However the occurrence of most of the phenomena that we will deal with regarding giant worm-like micelles does not depend critically on that specific nature. Accordingly, we shall henceforth rarely mention details of the chemical composition of the surfactant.

Although some surfactant micelles can form spontaneously, their formation often requires addition of another constituent, whether plain salt, a counterion or a co-surfactant, ie a short alcohol chain. Then, both the concentration in surfactant and the concentration in the additive constituent affect the rheological properties of the solution.

1.2 Concentration Regimes

Let us now consider the effect of surfactant concentration in order to distinguish the diverse regimes in which micelles can be found.

[1] as a matter of fact, there exist examples of worm-like micelles with rheologic properties very close to surfactant micelles, but made of other "molecular bricks". For instance, block co-polymers are a more and more investigated alternative to surfactants [5].

The key idea of this section is the following: Whether individual micelles aggregate is to be understood as the result of a competition between entropy, which favours sparse particles or smaller aggregates, and hydrophilic/hydrophobic interactions. How they then pack can be comprehended in terms of steric effects, ie geometric constraints, and, if applicable, electric repulsions.

We shall start from very low surfactant concentrations and gradually move to higher values.

1.2.1 Propensity for an interfacial position

It can easily be understood that amphiphiles such as surfactants prefer a position at the interface between the solvent and the gas phase (provided that there is a free surface), with, say, their head groups in the solvent and their tails pointing outwards if the solution is aqueous. Having surfactants thus assembled at the interface lowers surface tension, hence their name (**surf**ace **act**ive age***nts***). However the number of molecules that can be packed at an interface is tiny [8]: assuming the typical distance between two surfactants on a completely packed interface is determined by electrostatic repulsions and thus equates the Bjerrum length ($7\mathring{A}$ in a water-based solution), a surface of $1m^2$ could not accommodate more than $3 \cdot 10^{-13}$ mol of such molecules. For the concentrations we will deal with, excess of surfactants close to the surface can therefore be neglected.

1.2.2 From sparse surfactants to micelles

At very small surfactant concentrations, the loss of entropy associated with the formation of an aggregate is too large, and the solution is almost exclusively composed of sparse surfactant molecules. Their chemical potential μ_1 can be expressed as:

$$\mu_1 = \mu_1^0 + kT \ \ln x_1$$

for small concentrations x_1 of sparse molecules, using customary notations. An analogous can be written for aggregates of n molecules, which we regard as single particles for the time being:

$$\mu_{aggregate\,(n)} = \mu^0_{aggregate\,(n)} + kT \ \ln x_{aggregate\,(n)}$$

where $x_{aggregate}$ is the concentration of aggregates (taken as a whole). The chemical potential μ_n of a single surfactant molecule in such an aggregate is then:

$$\mu_n = \frac{\mu^0_{aggregate\,(n)}}{n} = \mu_n^0 + \frac{kT}{n} \ \ln \frac{x_n}{n}$$

where x_n is the concentration of individual surfactants that are part of aggregates of size n.

Equating the chemical potential of sparse surfactants and that of molecules in n-aggregates yields:

$$x_n = n \left(\frac{x_1}{e^{\beta(\mu_n^0 - \mu_1^0)}} \right)^n \tag{1.2.1}$$

where $\beta \equiv 1/kT$. Now, let N be the micellar size (defined as a number of surfactant molecules) that minimizes the chemical potential μ_n^0. Evaluating expression 1.2.1 for $n = N$ gives:

$$x_N = N \left(\frac{x_1}{cmc} \right)^N$$

Here cmc denotes the critical micellar concentration $e^{\beta(\mu_N^0 - \mu_1^0)}$. Since $N \gg 1$, when the total surfactant concentration rises above the cmc, there is a sharp transition to a state with non-negligible concentration of micelles, called **dilute regime**. It must also be noted that the equilibrium between micelles and isolated surfactants is a dynamic one, the integration of surfactant monomers to micelles balancing the dissolution of integrated monomers in the steady state.

1.2.3 Type of aggregation

Before moving on to the next regime, let us consider the shape of the aggregates that are formed. The most intuitive way to determine how surfactants are packed was proposed by Israelashvili [9] and consists in defining a packing parameter $\alpha \equiv \frac{v}{a_0 l_c}$ as the ratio of the volume v occupied by the molecule, and the area a_0 occupied by each head group times the length l_c of the chain (refer to Figure 1.2.1 for the notations).

Equating the numbers of surfactants obtained by volume considerations and by surface considerations (the head groups pointing out of the micelles in a water-based solvent) in specific geometries, one finds constraints on the packing parameter α for each of those geometries. The following cases will be of interest for us:

- $\star$ $\alpha \leqslant 1/3$: spherical micelles are allowed, and it is the shape that is actually selected.
- $\star$ $1/3 \leqslant \alpha \leqslant 1/2$: micelles are cylindrical.
- $\star$ $1/2 \leqslant \alpha \leqslant 1$: micelles are structured in bilayers.

Although the global micellar shape is fixed, individual surfactants within micelles do not have fixed positional order; their organisation is fluid-like.

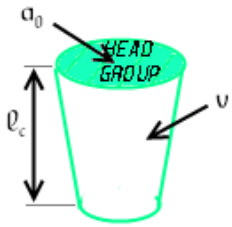

Figure 1.2.1: A surfactant molecule that is part of a micelle

One can now understand one of the reasons why the addition of salt or counterions is sometimes required to get cylindrical micelles. When free ions are added, screening surface charges becomes easier insofar as it costs less entropy. Consequently, the Debye layer that is necessary to screen electric charges gets thinner [2]. Repulsions between electrically-charged head groups are thus shorter-ranged, therefore a_0 decreases. As a result, the packing parameter α increases, and this can induce a sphere-rod transition. If surfactants are charged, increasing their concentration may have the same effect.

1.2.4 Dependence of size on surfactant concentration

Let us now restrict our attention to cylindrical micelles and determine what controls their length.

Once again, we follow Israelashvili's analysis as it is presented in [10]. Every cylinder is closed with two hemispherical endcaps to avoid exposure of their lipophilic core to the solvent. Noting μ^0_{cap} the chemical potential of one of the n_{cap} molecules in the cap and $\mu^0_{cylinder}$ that of a surfactant in the cylinder itself (this potential is assumed independent of the size of the micelle), the average potential of one surfactant in a micelle made of n molecules is:

$$\begin{aligned}\mu^0_n &= \mu^0_{cylinder} + \frac{n_{cap}}{n}(\mu^0_{cap} - \mu^0_{cylinder}) \\ &= \mu^0_{cylinder} + \frac{E_{sciss}}{n}\end{aligned}$$

Here $E_{sciss} \equiv n_{cap}(\mu_{cap} - \mu)$ is the excess of energy due to the caps, or, equivalently, the energy needed to break a cylindrical micelle into two parts, thereby creating two new caps. Its order of magnitude can be assessed to $n_{cap} \cdot 1kT \sim 10 - 20\,kT$ [7]. We now use Eq 1.2.1 to express the concentration of sparse surfactants x_1 as a function of the total surfactant volume concentration x:

$$\begin{aligned}x &= \sum_{n=1}^{+\infty} n \left(\frac{x_1}{e^{\beta(\mu^0_{cylinder} + E_{sciss}/n - \mu^0_1)}} \right)^n \\ &= e^{-\beta E_{sciss}} \sum_{n=1}^{+\infty} \sum_{k=1}^{n} \left[x_1 e^{\beta(\mu^0_1 - \mu^0_{cylinder})} \right]^n \\ &= e^{-\beta E_{sciss}} \frac{1}{[1 - x_1 e^{\beta(\mu^0_1 - \mu^0_{cylinder})}]^2}\end{aligned}$$

Basic algebraic manipulation then gives: $x_1 = (1 - \frac{1}{\sqrt{x \exp\left(\frac{+E_{sciss}}{kT}\right)}}) \exp\left(\frac{\mu^0_{cylinder} - \mu^0_1}{kT}\right)$

The distribution of size appearing in Equation 1.2.1 then turns into:

[2] it actually scales as $\lambda_D = \sqrt{\frac{\epsilon_0 \epsilon_r kT}{e^2 \sum z_i^2 c_i}}$, where $\epsilon_0\epsilon_r$ is the dielectric constant of the solution, e is the elementary charge, z_i the number of charges carried by ion i of concentration c_i

$$x_n = n \left[\frac{\left(1 - (x\, e^{\beta E_{sciss}})^{-1/2}\right)\, e^{\beta(\mu^0_{cylinder} - \mu^0_1)}}{e^{\beta(\mu^0_n - \mu^0_1)}} \right]^n$$

Finally, approximating $\left(1 - \frac{1}{\sqrt{x\, e^{\beta E_{sciss}}}}\right)^n$ with $\exp\left[\frac{-n}{\sqrt{x\, e^{\beta E_{sciss}}}}\right]$, one finds:

$$\boxed{x_n \simeq n\, e^{-n/N} e^{-\beta E_{sciss}};\quad N \equiv \sqrt{x}\, e^{\beta E_{sciss}/2}} \tag{1.2.2}$$

1.2.5 From dilute micelles to micellar entanglements

Having derived this formula[3], we turn to another regime, the **semi-dilute regime**, in which micelles start overlapping. This regime sets in as soon as the surfactant volume fraction reaches a critical value $x*$ for which the micellar radius of gyration R is approximately the average distance between two micelles. Let l_p be the persistence length of a micelle. Setting aside excluded volume effects (which is an arguable assumption in some cases), one gets $R \simeq l_p \sqrt{\frac{L}{l_p}}$ for a random walk of step l_p iterated $n = \sqrt{\frac{L}{l_p}}$ times. We assume that the contour length of a micelle is proportional to its size to respect volume conservation, ie $LS = Nv$, where S is the cylindrical cross-section area and v the volume occupied by an individual micelle. Thus $R = \sqrt{l_p \frac{Nv}{S}}$. At the critical micellar volume fraction $x*$, the radius of gyration R is equal to the average distance $(c*v)^{1/3}$ between micelles, ergo :

$$x* \simeq \left(\frac{S}{v^{1/3} l_p}\right)^{6/5} e^{-\beta E_{sciss}/5}$$

When the volume fraction reaches $x*$, a dramatic peak in the zero-shear rate viscosity is observed; in other words, to deform the nascent entanglement of micelles, large shear stresses are required.

At this stage one may find it suitable to enquire about the effect of salt concentration on the micellar sizes and the critical volume fraction. In Eq 1.2.2 giving the distribution of sizes, the energy cost E_{sciss} of two endcaps actually depends on the chemical nature of the surfactant and the salt, and on their respective concentrations. Indeed, different counterions do not have the same binding strength on a given surfactant micelle. For instance, in the case of CTAB, F^- and Cl^- are almost inefficient, $Br^-$is more strongly binding. NO_3^- is even more binding and displaces pre-existing Br^- from the direct vicinity of the micelles when it is added. Let us note that the above formula is valid for strongly binding counterions, and different expressions are presented in [5] for polyelectrolyte micelles whose counterions do not completely compensate the electrostatic charge.

Beyond these considerations of the specific nature of the chemical species, their concentration naturally has a great impact. As mentioned in section 1.2.3, higher salt concentration provides better

[3] other expressions are derived in [7] for branched micellar chains and micellar rings. In the latter case, a pleasant Bose-Einstein-like condensation on a giant macroscopic ring is found for large enough surfacant volume fractions.

screening of the charges, and therefore there is less need for the extra distance between surfactants created by curvature in the endcaps. Therefore E_{sciss} increases with salt concentration, as does the average micellar size (refer to Eq 1.2.2). As for the persistence length l_p, the same phenomenon, namely screening of charges lowering repulsions, effects a decrease of the persistence length. Adding salt can thus induce a rod-like to worm-like transition. Combining those antagonistic effects of increased salt concentration (on L and l_p) actually seems to lower the onset of overlapping $x*$, at least for relatively small salt concentrations [11].

From the semi-dilute to the concentrated regime and liquid crystals

The regime of **concentrated micelles** corresponds to a stage in which micellar length is no longer a critical parameter, because of the numerous entanglements between the micelles. We can say, for instance, that it sets in when the mesh size, ie the characteristic distance between entanglements, becomes lower than the persistence length. Let us note x^{**} the corresponding volume fraction of surfactant. Above x^{**}, micellar solutions then exhibit a lyotropic **liquid-crystal** behaviour, insofar as their organisation is dependent on their concentration x. At a given salt concentration,

- ⋆ For $x^{**} \leqslant x \leqslant x_{I-N}$, micelles are in an isotropic (I) state: no long-range order, whether orientational or positional, exists, entropy prevails and micellar chains are randomly entangled.
- ⋆ For $x_{I-N} \leqslant x \leqslant x_N$, a new phase appears and coexists with the isotropic phase. This new phase is called nematic (N) and features long-range orientational order, but no positional order: micelles align but, unlike in solid crystals, their position is not imposed by a given periodicity in space.
- ⋆ For $x_N \leqslant x \leqslant x_{other}$, there only remains the nematic phase.
- ⋆ For even higher values of surfactant concentration, other types of organisation are reported, from smectic-A to hexagonal and more exotic structures [10].

The isotropic-nematic (I-N) transition is related to our study of shear-banding because, as we shall see in Chapter II, it can be induced, not only by varying surfactant concentration, but also by imposing a shear flow.

As a conclusion for this section, Figure 1.2.2 presents a rough outline of the various micellar regimes encountered so far and their dependence on the surfactant and salt concentration.

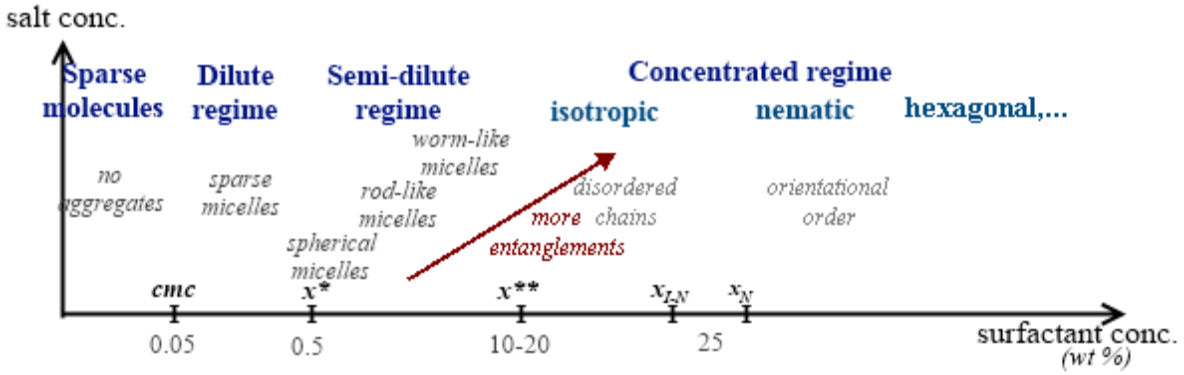

Figure 1.2.2: Schematic diagram of the different micellar regimes as a function of surfactant and salt concentration

1.3 Linear Rheology

This relatively short section is obviously not intended to encompass the whole breadth of linear rheology of worm-like micelles (presented e.g. in Ref [7]), nor does it target rigourous derivation of the few formulas it presents. Its aim is rather to offer a basic introduction to the physical mechanisms accounting for stress relaxation and the existence of normal-stress-differences that underpin the macroscopic approach used thereafter to address shear-banding in non-linear rheology.

1.3.1 The specificities of complex fluids

The rheological properties of worm-like micelles are those of a non-Newtonian fluid, or complex fluid. Let us first see how complex fluids differ from Newtonian ones. The latter are composed of disordered, isotropic[4] particles that can only dissipate energy and not store it. Thus, the flow does not affect the dynamics of the individual particles.

On the other hand, in so-called complex fluids, some organisational order often exists at the mesoscopic scale, because of e.g. the anisotropy or the finite size of the fluid particles. Such mesostructures may be rearranged due to the flow and therefore have a configurational energy, like in solids. Furthermore, at the microscopic scale, fluid particles of finite size may also store energy given by the flow. In other words, the latter affects their microscopic dynamics. A simple illustration for this[5] consists in imagining a microscopic spring immersed in the fluid. When a shear flow is imposed, the spring stretches, thereby storing elastic energy: the past strain has been stored in the fluid memory. This is the basis of the linear Maxwell model, whose precise equation will be derived in Chapter II.

[4] at least, at the scale of the flow

[5] simple though it might seem, this example has been the cornerstone of several major constitutive equations for complex fluids, some of which will be mentioned later on. The reason for this success is that stress results from interactions between particles, and these interactions can integrated in the spring's law, at least in theory. The whole point is naturally to properly determine this law and to define what springs'ends are.

It follows from this brief comparison between Newtonian and non-Newtonian fluids that under shear flow the normal stresses[6] τ_{ii}, τ_{jj} and τ_{kk} (with i, j and k the directions of the axes) of the former are equal, since the viscous shear stress has no normal component and the isotropic stresses have all their components equal by definition, whereas such an equality of normal stresses need not be in the case of the latter. In order to eliminate the isotropic pressure, one defines the following stress differences:

$$N_1 \equiv \tau_{11} - \tau_{22}$$
$$N_2 \equiv \tau_{22} - \tau_{33}$$

Here, *1* corresponds to the local velocity direction, *2* corresponds to the direction of the velocity gradient, and *3* corresponds to the neutral direction, ie the vorticity direction. Typically, one expects the normal stress in the direction of the flow to be the largest, and N_1 is positive. Most of the time, N_2 is negative and much smaller than N_1 in absolute value. This anisotropy affects the optical properties of the solution, for there exists a stress optical law which relates the difference in refraction indices according to the direction of polarization of light and the various stresses (and an extinction angle corresponding to the mean orientation of the anisotropic structures). Such a property is widely used in liqud crystal displays and, in rheology, in light scattering measurements and measurements of the flow birefringence.

1.3.2 Linear rheology

Let us now move on to linear rheology. Its principle consists in measuring the fluid response in terms of stress $\boldsymbol{\tau}$ (notably shear stress σ) to some (vanishingly) small strain γ. If the fluid is suddenly subjected to this strain at $t = 0$, the transient elastic modulus G is defined as the proportionality coefficient between shear stress and imposed strain:

$$\sigma(t) = G(t)\gamma$$

We now move back to our previous example of a spring, in other words to the Maxwellian model. Once some given deformation has been imposed and the spring has stretched, it starts relaxing towards its state of rest, while the energy it has stored is dissipated through viscous dissipation. Let us temporarily admit that the relaxation of energy follows a monoexponential decay with relaxation time λ_M, ie

$$G(t) = G_0 e^{-t/\lambda_M}$$

Instead of imposing a strain at time 0 and having the system relax, one can impose an oscillatory flow: $\gamma^*(\omega) \equiv \gamma_0 e^{i\omega t}$ in complex notations, where ω is the angular frequency. The complex modulus $G^*(\omega)$ obeying $\sigma^* = \gamma_0 e^{i\omega t} G^*$ can then be decomposed into a real part $G'(\omega)$ and an imaginary part $G''(\omega)$. $G'(\omega)$ controls an in-phase response, which is the storage of elastic energy, and is thus called storage modulus, whereas $G''(\omega)$ controls an out-of-phase response, namely, viscous dissipation, and is thus called loss modulus. For a liquid-like material, $\frac{G''}{G'} \gg 1$. An empirical rule, the Cox-Merz rule, relates the viscosity in oscillatory flow and the apparent viscosity in constant shear flow ($\eta(\dot{\gamma}) \sim \eta^*(\omega)$, with $\dot{\gamma}$ the applied shear rate, $\eta \equiv \frac{\sigma}{\dot{\gamma}}$ and $\eta^* \equiv \frac{G^*}{i\omega}$ the apparent viscosities).

[6] the normal stress τ_{ij} is defined as the i-component of the force $\overrightarrow{F}$ exerted on a unit area of the surface of normal $\overrightarrow{e_j}$: $\tau_{ij} dS_j = \overrightarrow{F} \cdot \overrightarrow{e_i}$

1.3.3 The reaction-reptation model

Linear rheology experiments have shown that worm-like micelles in the entangled regime and at high enough salt concentrations relax with a single characteristic time [10], as in the linear Maxwell model. However there are conspicuous hints that more physics is hidden behind this than there is in the Maxwell model insofar as polymer chains do not relax with a monoexpoential decay. In effect, a combination of two physical mechanisms involving living polymers was put forward by Cates [12] to explain this monoexponential decay.

Reptation

The first concept is *reptation* and it was introduced in the early 70's by de Gennes [13] for polymer chains. The occurrence of reptation in the case of worm-like micelles is thus in keeping with their polymeric nature.

As mentioned in section 1.3.1, the microscopic and mesoscopic structures of complex fluids can store energy, so stress does not vanish at once when strain is no longer imposed. If a polymer chain were remote from the other chains in the solution, the imposed strain would elongate the polymer chain, that is, increase the end-to-end distance of the chain; then, when the applied strain comes back to zero, the polymer would relax quickly (compared to the actual relaxation time) to its rest state, on account of its nature of entropic spring that favours an average end-to-end distance equal to zero. But in the regime under study our polymer is not isolated and entanglements with other chains act as obstacles on its way back to its state of rest. Indeed, the presence of other chains confines our polymer to some fictitious tube. This tube is represented in 2D in Figure 1.3.1 for entangled polymers perpendicular to the plane of motion of our polymer.

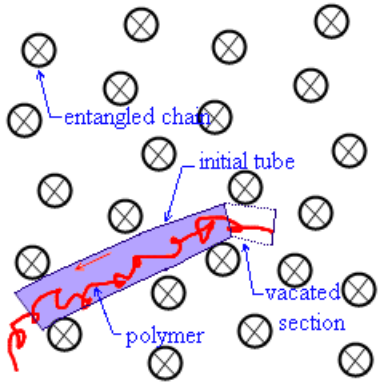

Figure 1.3.1: Artist's impression of the reptation process

We assume that the relaxation of our polymer within any section of its wrapping tube is much faster than relaxation along the tube, the latter occurring only through curvilinear diffusion (reptation), with coefficient $D_c \propto 1/L$. We can therefore consider that stress survival is caused by the confinement imposed by the initial tube, which keeps track of the deformation. As soon as the polymer escapes

from a section of this tube, all the stress this section used to bear vanishes[7]. Considering the total stress as the sum of the stresses in every tube section, one gets the following expression for the transient elastic modulus (defined in section 1.3.2):

$$G(t) = G_0\mu(t)$$

where $\mu(t)$ is the fraction of the initial tube still surviving at time t. A nice probabilistic argument then gives the dependence of μ on t [7]: let us sit in the frame of the polymer chain and assimilate a given tube section to a free particle diffusing on a segment of length L. Once the free particle reaches an extremity of this segment, ie one of the ends of the polymer, it dies, because the stress the corresponding section bears vanishes. $\mu(t)$ is then the survival probability of the free particle at time t, which a probability calculation evaluates to:

$$\mu(t) = \sum_{n\,odd} \frac{8}{n^2\pi^2} \exp(-n^2 t/\tau_R)$$

where $\tau_R(L) \equiv \frac{L^2}{\pi^2 D_c} \propto L^3$. The slowest relaxation times are the $\tau_R(L)$, but given that polymers of various lengths coexist, this gives a combination of many different relaxation times (and not a monoexponential decay).

Reaction

The second concept is reaction and its combination with reptation was proposed by Cates [12] in the late 90's. It stems from the living nature of worm-like micelles, that is, their capacity to break and recombine.

Different types of breaking and recombining events can be envisaged, but we arbitrarily choose to restrict our attention here to reversible scission: a micelle breaks into two parts (and the converse recombination). Let us divide the micelle into small sections along its axis. Each pair of adjacent, connected sections has the same breaking rate $k_{rs}^{section}$, and thus has survival probability $e^{-k_{rs}^{section}t}$. Changing units so that a section has unitary length, there are L such pairs in the micelle, with L the micellar length. Then the whole micelle has survival probability $[e^{-k_{rs}^{unit}t}]^L$, and the characteristic time for breakage is thus:

$$\tau_{rs} \equiv \frac{1}{L\,k_{rs}^{unit}}$$

Analogous characteristic times can be derived for the other breaking processes, the shortest of those times is denotes τ_b. Very roughly speaking, after each time step τ_b, two new chain ends are created and their diffusive motion helps relax stress, as well as the diffusive motion of the initial chain ends did.

To bring reptation intto the present picture, let us consider the limit $\tau_b \ll \tau_R$. Consider some tube section. In the limit considered here, the micelle escapes from that section if breakage occurs in its vicinity and one of the newly-created chain ends then reptates through it. The distance a chain

[7] the newly-created tube section is not supposed to bear stress since it is formed in a state of rest

end reptates during its lifetime τ_b (which is the breaking time as well as the recombining time at equilibrium) is approximately $l \simeq \sqrt{D_c \tau_b}$. The number of breakages required before the section is vacated is of order L/l, so the waiting time is

$$\tau \equiv \frac{L\sqrt{\tau_b}}{\sqrt{D_c}} \sim \sqrt{\tau_b \tau_R}$$

τ is a function of L, because so are τ_b and τ_R. But if $\tau_b \ll \tau$ the micellar length is randomized a large number of times before the tube section is vacated. Accordingly τ is averaged over the various lengths L and is thus almost independent of the initial micellar length. It follows that all tube sections relax with the same characteristic time, hence the monoexponential decay !

Chapter 2

Shear-banding: Physics & Numerics

The previous part has shed light on some significant discrepancies between polymers and giant-wormlike micelles. Those differences naturally impact their rheological properties. In particular, experimental observations of worm-like micellar solutions in shear flow have unveiled an intriguing phenomenon, unprecedented with polymer solutions: the flow curve $\sigma = f(\omega)$, where σ is the shear stress and ω is the applied shear rate, measured in, say, a cone-and-plate device[1], grows at low ω, which is expected, but then displays a stress plateau, that is, the shear stress remains constant while the velocity on the wall, hence the applied shear rate, are increased. The present section aims at exploring the physics of this singular behaviour, called shear-banding, which remained mysterious until some 20 years ago. We will alsodescribe how we haved proceeded to simulate it numerically.

2.1 Presentation of some constitutive models

Some microscopic mechanisms occurring in linear rheology have been presented above, and a few microscopic models have been developed for worm-like micellar solutions. However their intricacy makes them intractable for solving complex non-linear phenomena, such as shear-banding. Indeed, the latter occurs in constant shear flow, which is intrinsically non-linear, for the integration of the strain rate over time gives huge deformations, even at low shear rates. In order to deal with non-linear rheology, microscopic models are therefore usually substituted by macroscopic or phenomenological approaches, whose success is assessed with respect to their capacity to capture experimental data or observations, much more than to the solidity of their microscopic foundations.

[1] cone-and-plate rheometry is presented in Chapter VI

2.1.1 Linear Maxwell fluid

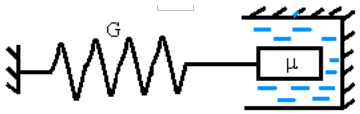

Figure 2.1.1: Representation of a Maxwell fluid

Let us come back to our example of a spring immersed in a solution. Let us clearly distinguish elastic effects from viscous effects linked with the surrounding fluid. The latter are modelled by a dashpot, ie a hydraulic damper. Connect the spring and the dashpot in series. The balance of force on the damper (supposed inertialess) gives:

$$\boldsymbol{\tau} + 2\mu\mathbf{e_f} = \mathbf{0} \tag{2.1.1}$$

where $\boldsymbol{\tau}$ is the stress exerted by Hookean (multidimensional) spring, μ is the fluid viscosity and $\mathbf{e_d}$ is the strain rate tensor of the fluid relative to the . Let $\boldsymbol{\epsilon_t}$ be the strain tensor and $\dot{\boldsymbol{\epsilon}}_\mathbf{t}$ its time derivative. The strain rate tensor of the dashpot relatived to the fixed wall is $\mathbf{e} = -\mathbf{e_f} + \dot{\epsilon}_\mathbf{t}$. The Hookean force can be written: $\boldsymbol{\tau} = G\boldsymbol{\epsilon_t}$. Then Eq 2.1.1 can be reformulated as:

$$\boldsymbol{\tau} + \lambda_M \dot{\boldsymbol{\tau}} = 2\mu\mathbf{e}$$

where $\lambda_M \equiv \frac{2\mu}{G}$ is the relaxation time of the linear Maxwell fluid. The above equation proves that a Maxwell fluid has a single relaxation time in a shear-stop experiment.

2.1.2 Upper Convected Maxwell and Oldroyd-B models

The Maxwell model has one major drawback: it does not respect the principle of frame indifference. Indeed, the time derivative of the stress tensor $\boldsymbol{\tau}$ should take into account rotation and elongation of the axes as a material volume unit is moving. To respect this principle, the time derivative $\frac{\mathfrak{D}\boldsymbol{\tau}}{\mathfrak{D}t}$ of the stress tensor should include:

- ⋆ an advection term accounting for the displacement of the centre of gravity of the "fluid particle" (or, if one prefers, the material volume unit): $v \cdot \nabla\boldsymbol{\tau}$
- ⋆ a term accounting for the extension of the axes[2] : $-Sym(\boldsymbol{\tau}\cdot\mathbf{e})$, where Sym denotes the symetric part $\frac{\mathbf{D}+{}^\mathbf{t}\mathbf{D}}{2}$ of a tensor D and $\mathbf{e}$ is the symetric part of the velocity gradient ∇v
- ⋆ a term accounting for the rotation of the axes: $-Sym(\boldsymbol{\tau}\cdot\boldsymbol{\omega})$, where $\boldsymbol{\omega}$ is the antisymetric part of the velocity gradient

[2] in the upper convected derivation. The expression is different in the lower convective derivation.

Since $\nabla v = \boldsymbol{\omega} + \mathbf{e}$, the polymer stress obeys:

$$\boldsymbol{\tau} + \lambda_M \left[\frac{\partial \boldsymbol{\tau}}{\partial t} + v \cdot \nabla \boldsymbol{\tau} - Sym(\boldsymbol{\tau} \cdot \nabla v) \right] = 2\eta_p \mathbf{e} \tag{2.1.2}$$

Here, η_p is the polymeric viscosity. If no solvent viscous stress is added, the combination of Eq 2.1.2 with the Navier-Stokes equations, where the polymeric stress $\boldsymbol{\tau}$ is inserted, yields the Upper Convected Maxwell model.

If a solvent contribution to stress is added, the total stress becomes: $\mathbf{T} = \boldsymbol{\tau} + 2\eta_s \mathbf{e}$ (let us note that η_s is called the solvent viscosity, but in fact it represents the Newtonian contribution of the whole fluid to the shear stress, so its value does not have to match the viscosity of the unmixed solvent). This is the famous Oldroyd-B model, which descibes the rheology of dilute polymer solutions fairly well.

The latter model can actually be derived from a microscopic model consisting of a dilute suspension of dumbbelles, ie beads connected by a Hookean spring.

Under shear flow, if $\dot{\gamma}$ is the local shear rate, ie $\nabla v = \begin{pmatrix} 0 & 0 \\ \dot{\gamma} & 0 \end{pmatrix}$ in two dimensions, the following formulas can be derived for the total shear stress Σ and the normal-stress-differences:

$$\Sigma = (\eta_p + \eta_s)\dot{\gamma}$$

$$N_1 = 2\,\lambda_M \eta_p \dot{\gamma}^2$$

$$N_2 = 0$$

2.1.3 Johnson-Segalman model

One major theoretical failure of the Oldroyd-B model is to allow infinite extension of the Hookean springs, which have a linear response to extension. This can be overcome by imposing a maximal value for extension; this approach resulted in finite-extension models such as FENE-P.

An alternative consists in allowing slip on the beads via a slip-parameter[3] $a \in [-1, 1]$, which leads to non-affine deformation of the spring. Adding a solvent contribution through solvent viscosity η_s like in Oldroyd-B, one finds the Johnson-Segalman model:

$$\boxed{\boldsymbol{\tau} + \lambda_M \left[\frac{\partial \boldsymbol{\tau}}{\partial t} + v \cdot \nabla \boldsymbol{\tau} - (1+a)\, Sym(\boldsymbol{\tau} \cdot \nabla v) + (1-a)\, Sym(\nabla v \cdot \boldsymbol{\tau}) \right] = 2\eta_p \mathbf{e}} \tag{2.1.3}$$

In this model, the total shear stress Σ and the normal-stress-differences, plotted in Figure 2.1.2, obey:

[3] Taking $a = 1$ gives the Oldroyd-B model

$$\Sigma = \frac{\eta_P \dot{\gamma}}{1 + (1 - a^2)\lambda_M^2 \dot{\gamma}^2} + \eta_s \dot{\gamma}$$

$$N_1 = \frac{2\lambda_M \eta_P \dot{\gamma}^2}{1 + (1 - a^2)\lambda_M^2 \dot{\gamma}^2}$$

$$N_2 = \frac{-(1 - a)\lambda_M \eta_P \dot{\gamma}^2}{1 + (1 - a^2)\lambda_M^2 \dot{\gamma}^2}$$

Like in other models, only little physics is involved in the Johnson-Segalman one. However for a well selected parameters, more precisely $\eta_P/\eta_s > 8$ and $a < 1$, it has a major, surprising feature: the micellar shear stress σ tends to zero at infinite shear rates and the flow curve $\Sigma = f(\dot{\gamma})$ is non-monotonic. A region of negative slope thus spans the range of shear rates between, say, $\dot{\gamma}_1$ and $\dot{\gamma}_2$ (dashed in Figure 2.1.2); it results from the alignment of the microscopic dumbbells with the flow and their subsequent disentanglement, which effect a decay of the polymeric shear stress. Consequently, in the limit high shear rates, the fluid is purely Newtonian, with viscosity η_s. Such non-monotonicity gives rise to a rich phenomenology, close to experimental observations. It may also be noted that the first normal-stress-difference is bounded: slip on the beads prevents them from generating infinite stresses.

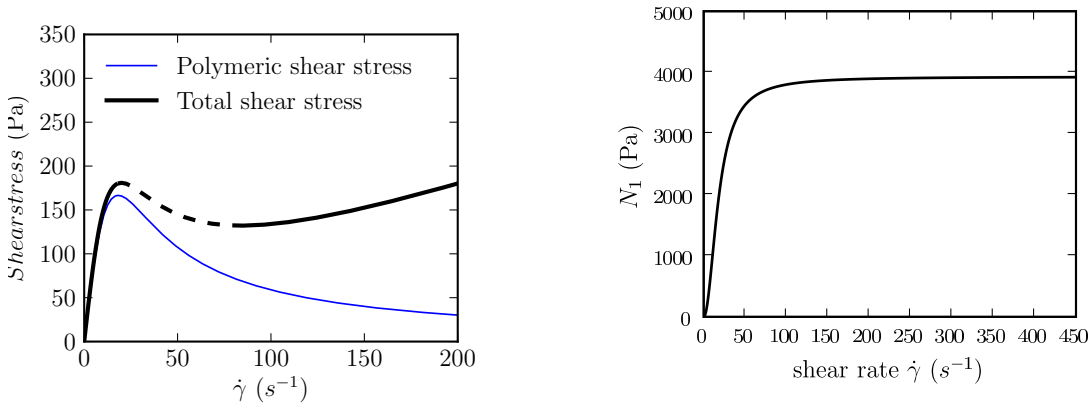

(a) Total shear stress

(b) First normal-stress-difference

Figure 2.1.2: Dependence of (a) the shear stress (b) the first normal-stress-difference on the local shear rate in the Johnson-Segalman model

2.2 Unstable regions and shear-banding

From now on, we will exclusively consider the non-monotonic Johnson-Segalman model, in the Stokesian regime, that is, without inertia.

2.2.1 Planar geometry

Let us first condider an ideal planar geometry[4] consisting of two infinite parallel plates, one of which is translated at velocity V (see Figure 2.2.1 for the notations). Let d be the distance between the plates.

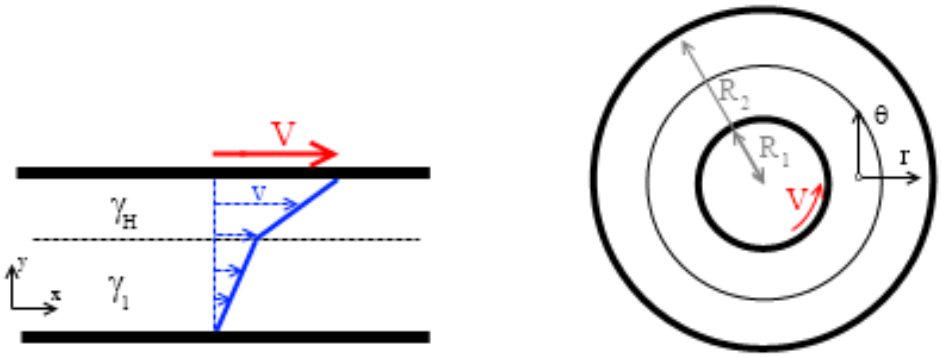

(a) Planar geometry (b) Taylor-Couette geometry

Figure 2.2.1: Different geometries

Regions of negative slope $\frac{d\Sigma}{d\dot{\gamma}}(\dot{\gamma}) < 0 \ \forall \dot{\gamma} \, in \, [\dot{\gamma}_1, \dot{\gamma}_2]$ in a non-monotonic flow curve are known to be mechanically unstable. We will not present any proof for this well-established result, except the following rather intuitive reasoning: Consider a gap with applied shear rate $\omega \equiv \frac{V}{d} \, in \, [\dot{\gamma}_1, \dot{\gamma}_2]$. Variables are assumed to depend only on the gap coordinate y, which imposes a flow parallel to the plates. Suppose the flow is homogeneous, with uniform local shear rate $\dot{\gamma} = \omega$. A small increase of the local shear rate will reduce the shear stress. This increase may then propagate up to the walls. However, on the wall, some given velocity is imposed, so a region of lower shear-rate needs to be created to match the boundary condition. This can be achieved without increasing the local shear stress since the latter is multivalued, ie another (lower) shear rate exists at the same shear stress.

The system finally reaches a shear-banded state, where one (or more) band of low shear rate $\dot{\gamma}_l$ coexists with one of high shear rate $\dot{\gamma}_H$. Both shear rates are located on stable regions of the flow curve for stability reasons and, since div $T = 0$ implies $\frac{d\Sigma}{dy} = 0$, they have to obey

$$\Sigma(\dot{\gamma}_l) = \Sigma(\dot{\gamma}_H) \tag{2.2.1}$$

In planar geometry, the interface between the bands is parallel to the plates and the shear rate is constant in each of the bands.

The proportion of the high- and low-shear bands has to ajust so as to obey the condition of integration $V = \int \dot{\gamma}(y) \, dy$, which gives the so-called lever-rule:

$$\boxed{\alpha_H \dot{\gamma}_H + (1 - \alpha_H)\dot{\gamma}_l = \omega}$$

where $\omega \equiv \frac{V}{d}$ is still the applied shear rate and α_H is the high-shear-band proportion.

[4] in practice, this geometry is approaches in some respects in a cone-and-plate rheometer. See Part VI.

Before we turn to the Taylor-Couette geometry, let us remark that, so far, nothing imposes the value of the shear stress in the shear-banded system as long as it satisfies the shear stress balance given by Eq 2.2.1. In order to have a shear-banded system, shear stress thus needs to be multivalued in $\dot{\gamma}$.

Let us also note that, beside the mechanical explanation for shear-banding, there is also a dual, thermodynamical explanation. Both are naturally not incompatible. In the latter viewpoint, shear-banding is regarded as a shear-induced phase transition from an isotropic to a nematic phase: the nematic order in the high-shear band and the strong orientation of the micelles it involves account for the lower apparent viscosity of this band, as compared with the highly-entangled, isotropic low-shear band. There is robust experimental evidence from small-angle X-ray scattering (SAXS) [14], small-angle neutron scattering (SANS) [5], nuclear magnetic resonance (NMR, following the pioneering works of Callaghan in this field [15]) and flow birefringence [5] experiments, showing that the high-shear band in concentrated systems close to the I-N transition are rest is indeed nematic. For systems in the semi-dilute regime, the situation is slightly more ambiguous [2].

2.2.2 Taylor-Couette geometry

The global picture in planar geometry is slightly modified by curvature effects in Taylor-Couette geometry, that is, for flows between two concentric cylinders (see Figure 2.2.1 for details of the notations). Only the inner cylinder will be rotated in our inquiry).

The local stress balance div $T = 0$ in the creeping regime implies

$$\Sigma(r) = \frac{R_1^2}{r^2}\Sigma(R_1) \tag{2.2.2}$$

Thus shear stress is inhomogeneous and the local shear rate in each band is not constant. Besides, the shear stress is a function of the local shear rate; in other words,

$$\frac{R_1^2}{r^2}\Sigma(R_1) = f[\dot{\gamma}(r)]$$

where f is a function defined by model parameters. As long as $\frac{R_1^2}{r^2}\Sigma(R_1)$ has two "stable" pre-images by f, say, $\dot{\gamma}_l$ and $\dot{\gamma}_H$, the local shear rate can switch between those values across the plateau; in order to respect the integral condition giving the velocity on the inner wall, only the total proportion of the high-shear band will need to be adjusted[5].

Consequently, for some range of applied shear rates, there will be a continuum of possible torques measured on the inner wall and no constraint on the number of bands.

This picture is somewhat puzzling and it so happens that it disagrees with experiments: what is measured is a robust selection of a given shear stress at each point on the plateau, and only two shear bands are observed.

[5] A more detailed analysis can be found in [17].

2.3 Insertion of a diffusive term, stress selection

2.3.1 Microscopic origin

The Johnson-Segalman (JS) model as exposed in Eq 2.1.3 contains only local terms, which means that no diffusive motion across streamlines is taken into account: streamlines are totally independent of one another. One might question the physical relevance of such independence.

As El Kareh and Leal have shown [19], Brownian motion is actually already included in the microscopic derivation of the JS model. It acts upon both the centre of mass of the dumbbell and its end-to-end distance. However, the difference in the velocity of the beads is obtained using a linearization, notwithstanding the fact that nothing in the equations prevents the velocity field from varying in a non-linear fashion at the scale of a dumbbell. Rejecting this linearization, the authors derived a Fokker-Planck equation for the stochastic dynamics and found a new, non-local term in the constitutive equation. This gives the diffusive Johnson-Segalman model:

$$\boldsymbol{\tau} + \lambda_M \left[\frac{\partial \boldsymbol{\tau}}{\partial t} + v \cdot \nabla \boldsymbol{\tau} - (1+a)\, Sym(\boldsymbol{\tau} \cdot \nabla v) + (1-a)\, Sym(\nabla v \cdot \boldsymbol{\tau}) \right] = 2\eta_p \mathbf{e} + l^2 \nabla^2 \boldsymbol{\tau} \qquad (2.3.1)$$

where l is a diffusive length. Velocity and stress profiles are now smoothened by diffusion and the interface between adjacent bands acquires finite width.

Nevertheless no estimate of the value of l is given by theory. In this regard, the diffusive term introduced in the model is somewhat arbitrary and in good part phenomenological.

2.3.2 Selection of a unique stress

The aim of the rest of this section is now to prove that the addition of a diffusive term, which changes the nature of the equation from hyperbolic to parabolic, enforces unique stress selection at the interface.

Radulescu and co-workers [18] propose an elegant analysis in the case of a plane flow where only the shear stress plays a role (meaning it is decoupled from the normal stresses). The fundamental idea is the following: across the interface, there is a "smooth jump" in the polymeric shear stress. Thus there is continuous Brownian motion of dumbbells (or micellar chains) carrying different micellar shear stresses to-and-fro across the interface. Since the total shear stress at the interface controls the relaxation time (in their one-stress-component model), if it does not have the proper value Σ^*, the balance between diffusion and relaxation across the interface will be broken: if, say, chains from the low-shear-band relax too quickly, the interface will move towards the low-shear band to reestablish the balance.

In terms of equations, using the same notations as above, we can write a generic form of the constitutive relation:

$$\partial_t \sigma = g(\sigma, \frac{\Sigma - \sigma}{\eta_s}) + l^2 \partial_y^2 \sigma \qquad (2.3.2)$$

Here, the shear rate has been substituted by $\frac{\Sigma-\sigma}{\eta_s}$ and g is some function depending on the model. Let y^* be the interface position and $\tilde{y}$ the co-moving frame coordinate: $\tilde{y} \equiv y - y^*(t)$. The derivation with respect to time can thus be replaced by a derivation with respect to $\tilde{y}$. Eq 2.3.2 then turns into:

$$l^2 \partial_{\tilde{y}}^2 \sigma = -g(\sigma, \frac{\Sigma - \sigma}{\eta_s}) - c\,\partial_{\tilde{y}}\sigma \tag{2.3.3}$$

where $c \equiv \frac{dx^*(t)}{dt}$. The whole point is now to recognize in Eq 2.3.3 a version Newton's second law for the movement applied to a fictitious particle of mass l^2 and of position σ. In this analogy, $\tilde{y}$ plays the role of time, $V(\sigma, \Sigma) \equiv \int g(\sigma, \frac{\Sigma-\sigma}{\eta_s})\, d\sigma'$ is a potential and $c\,\partial_{\tilde{y}}\sigma$ is a friction force. Finally, writing that the potential energy difference across the interface is dissipated by friction yields:

$$c = 0 \;\Leftrightarrow\; \int_{\dot{\gamma}_l}^{\dot{\gamma}_H} \frac{\partial g}{\partial \sigma} d\dot{\gamma} = 0$$

In other words, the interface is stationary and the system is stable if, and only if, some integral is zero. This integral is actually very close to Maxwell's integral condition: $\int_{\dot{\gamma}_l}^{\dot{\gamma}_H} [\Sigma(\dot{\gamma}) - \Sigma^{interface}] d\dot{\gamma}$, where $\Sigma(\dot{\gamma})$ is the total shear stress in the diffusionless JS model. Figure 2.3.1 shows a geometric interpretation for the latter condition, which proves that diffusion contributes to the selection of a unique total shear stress Σ^*at the interface, independently of the diffusion coefficient.

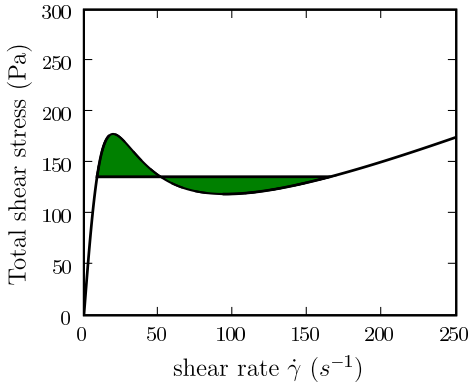

Figure 2.3.1: Geometric interpretation of Maxwell's integral condition. The regions filled with green above and below the constitutive flow curve have the same area. Σ^* corresponds to the horizontal line.

In the planar case, the total shear stress Σ is uniform across the gap, so $\Sigma = \Sigma^*$takes a given value as soon as shear-banding occurs. This accounts for the stress plateau in the flow curve (see Figure 2.4.1).

In Taylor-Couette geometry, curvature imposes the following relation between the stress at the interface r^* and that measured on the inner wall R_1, according to Eq 2.2.2

$$\Sigma(R_1) = \frac{r^{*2}}{R_1^2}\Sigma^*$$

When the applied shear rate increases, the proportion of the high-shear band increases, so the interface moves from the inner cylinder to the outer cylinder. Accordingly, r^*increases and $\Sigma(R_1)$, which is proportional to the torque measured on the inner cylinder, increases too. Hence the small slope on the plateau, of order $\left(\frac{R_2}{R_1}\right)^2 \frac{\Sigma*}{\dot{\gamma}_H - \dot{\gamma}_l}$. Larger slopes are however observed, but their explanation lies without the framework of the JS model and can be sought for instance in micellar concentration differenes between the bands.

2.4 Numerical simulation of a shear-banded system

In this section, we expose how we have proceeded to simulate a base shear-banded flow in a Taylor-Couette geometry, with a relatively small gap.

2.4.1 Fitting of the model parameters

To select physically-relevant model parameters, we fit experimental data, namely the first normal-stress-difference N_1 and the total shear stress Σ, collected by S. Lerouge and co-workers on a cone-plate rheometer using cetyltrimethylammonium bromide (CTAB) at 0.3M mixed with sodium nitrate $NaNO_3$ at 0.405M. The experimental shear stress profile dispays a shear-banding plateau between applied shear rates $\omega_l \simeq 10s^{-1}$ and $\omega_h \simeq 120s^{-1}$. As reported in [3], there appears to be a change in slope around $\omega_l \simeq 80s^{-1}$. It will be disregarded, since our DJS model is unable to account for it.

Figure 2.4.1 shows the experimental, constitutive and simulated curves, with the following model parameters: $a = 0.985$, $\lambda_M = 0.3227s$ (to be compared with the value of 0.23s given by linear rheology for the same system), $\eta_p = 18.2\, Pa \cdot s$, $\eta_s = 0.60\, Pa \cdot s$, which are the best fitting we were able obtain. For reasons to be explained in PartVI, values of N_1 on the plateau are not te be taken into account.

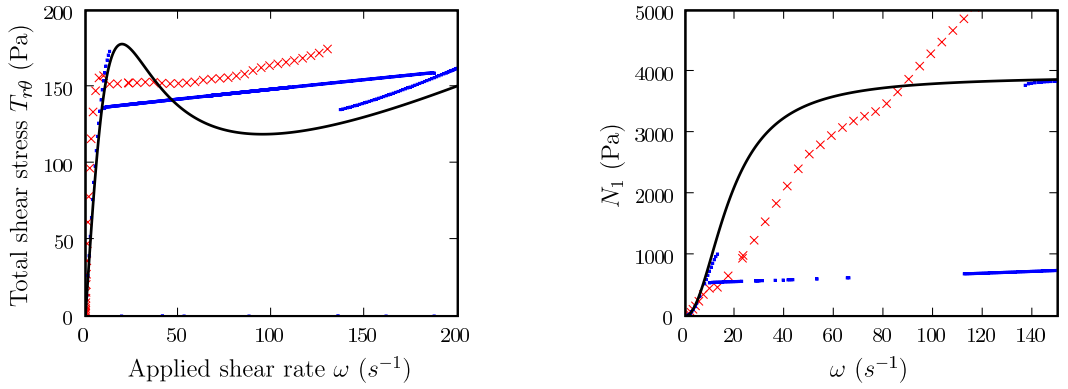

(a) (b)

Figure 2.4.1: Fitting of model parameters for (a) the total shear stress and (b) the first normal-stress-difference. Red cross (×): experiments, black line: constitutive curve for JS model, blue circles (○): simulations ($l = 10^{-3}R_1$)

As for the diffusive length, it has to be more than the mesh size, approximately 10 nanometers, and there is some experimental evidence suggesting it is between 1 and 10 micrometers. We will mainly focus on the cases $l = 10^{-3}R_1 \approx 13\mu$m and $l = 10^{-3.5}R_1 \approx 4\mu$m.

2.4.2 Rescaled equations

From now on, we will work with adimensional variables. Eq 2.3.1 takes the following adimensional form[6]:

$$\tilde{\boldsymbol{\tau}} + Wi[\frac{\partial \tilde{\boldsymbol{\tau}}}{\partial t} + \tilde{v}\cdot\tilde{\boldsymbol{\nabla}}\tilde{\boldsymbol{\tau}} - (1+a)\,Sym(\tilde{\boldsymbol{\tau}}\cdot\tilde{\boldsymbol{\nabla}}\tilde{v}) + (1-a)\,Sym(\tilde{\boldsymbol{\nabla}}\tilde{v}\cdot\tilde{\boldsymbol{\tau}})] = 2\,\mathbf{e} + \tilde{l}^2\tilde{\Delta}\tilde{\boldsymbol{\tau}} \tag{2.4.1}$$

where lengths have been rescaled with the radius R_1 of the inner cylinder, velocities with $\frac{\Omega R_1}{\epsilon(2+\epsilon)}$ ($\epsilon = {}^{1.13}/_{13.33}$ being the non-dimensional gap width), stresses with $\frac{\eta_P\Omega}{\epsilon(\epsilon+2)}$, pressure with $p = \frac{(\eta_P+\eta_s)\Omega}{\epsilon(\epsilon+2)}$ and the Weissenberg number, which compares the relaxation time and a characteristic shear time, has been defined as follows: $Wi \equiv \frac{\lambda_M\Omega}{\epsilon(2+\epsilon)}$. For simplicity's sake, we shall omit the tildes hereafter.

We impose the following boundary conditions on the walls:

- ⋆ no wall-slip for the velocity, ie $v(1) = V_{inner\,cylinder} = \epsilon(2+\epsilon)$ and $v(1+\epsilon) = 0$
- ⋆ no stress flux across the wall, ie $\nabla\tau_{ij}\cdot\vec{n} = 0\ \forall i,j$, where $\vec{n}$ is the normal to the wall

No boundary condition is imposed on the cylinder caps in the vorticity direction.

For the base flow, only dependence on the r-coordinate is kept. By virtue of symmetry, the flow is then purely azimuthal. Even with this simplification, the projection of the DJS equation 2.4.1 on every tensor component yields four rather long expressions, namely, three for the micellar stress and one for the azimuthal Navier Stokes equation; the interested reader can find those expressions in Appendix A.

2.4.3 Asymptotic expansion and space discretization

Let us envisage an asymptotic expansion of DJS Eq 2.4.1. Two kinds of regions appear:

- ⋆ two regions on both sides of the interface, one in the vicinity of the inner cylinder, the other in the vicinity of the outer cylinder. Those regions are respectively the high- and low-shear bands. In the approximation of zero curvature, the shear rate is constant in each of those bands. Therefore the space derivatives of the stress tensor are negligible.

[6] Better and more sophisticated rescalings have been proposed (e.g. in [18]), but this one is sufficient for our purpose

- ⋆ an interfacial region around the interface, where the space derivative of the micellar stress tensor are large. The width of this region is of order l, which is intended to be very small (less than 10^{-3} whereas the gap width is $\epsilon \approx 0.1$)

As a matter of fact, we do not plan to carry out the asymptotic expansion any further. Yet, it was not useless, since it has revealed that there is a very narrow region, the interfacial one, where derivatives are very large. Consequently, this region requires very fine resolution. Instead of discretizing indiscriminately a single region spanning the gap, we are therefore led to divide the gap into the three above domains and discretize each of them separately. This gives birth to a Multidomain code.

2.4.4 Numerical method

We have used a pseudospectral method. This method consists in getting derivatives via spectral analysis, but keeping real time.

More precisely, for spatial dependences, collocation points $r_1, r_2, \ldots, r_M$ are spread throughout the gap with a sine density in each domain. A given function c is represented by a vector

$$\widehat{C} = \begin{pmatrix} c(r_1) \\ c(r_2) \\ \vdots \\ c(r_M) \end{pmatrix}$$

containing its values at the collocation points. Its space derivative is then obtained by multiplication with a Tau-Chebyshev matrix[7] $\mathbf{D}_{MD}$ adapted to our multidomain code: $\frac{dV}{dr} = \mathbf{D}_{MD} \cdot V$.

We then take advantage of the fact that the Navier-Stokes equation

$$0 = \tau'_{r\theta} + \frac{2}{r}\tau_{r\theta} + \frac{\eta_S}{\eta_P}[v''_\theta + \frac{v'_\theta}{r} - \frac{v_\theta}{r^2}]$$

is partly decoupled from the other equations to eliminate v_θ from the other equations. First, we write

$$\left(\mathbf{D}_{MD} + 2\widehat{R^{-1}}\mathbf{II}\right)\widehat{\tau_{r\theta}} = -\frac{\eta_s}{\eta_p}\left(\mathbf{D}_{MD}^2 + \widehat{R^{-1}} \cdot \mathbf{D}_{MD} - \widehat{R^{-2}}\mathbf{II}\right)\widehat{V_\theta} \tag{2.4.2}$$

where $\mathbf{II}$ is the identity matrix.

The two boundary conditions on the velocity are implemented by replacing two rows of the matrix multiplying $\widehat{V_\theta}$ on the right-hand side of Eq 2.4.2 by $\begin{pmatrix} 1 & 0 & \ldots & 0 \end{pmatrix}$ and $\begin{pmatrix} 0 & 0 & \ldots & 1 \end{pmatrix}$, emptying the corresponding rows on the right-hand side and adding a constant vector containing only the

[7] the Tau-Chebyshev matrix results from spectral analysis, which implies that its components are non-zero even far from the diagonal.

boundary conditions, ie two non-zero components. After inversion of the left-hand-side matrix, we get a linear relation between $\widehat{\tau_{r\theta}}$ and $\widehat{v_\theta}$, involving some well-defined matrix $\boldsymbol{C}$:

$$\widehat{v_\theta} = \mathbf{C} \cdot \widehat{\tau_{r\theta}}$$

Now, the other three equations can be expressed as follows

$$\widehat{\tau} \equiv \begin{pmatrix} \widehat{\tau_{rr}} \\ \widehat{\tau_{r\theta}} \\ \widehat{\tau_{\theta\theta}} \end{pmatrix}$$

$$\partial_t \widehat{\tau} = \phi\left(\widehat{\tau}\right)$$

For the time derivatives, we first used an explicit Euler numerical scheme, but it performed relatively poorly for at least two reasons. First the DJS equations resemble a heat equation, and we therefore expect an upper bound on the valid time steps Δt. Then, the transient is quite long, as it has been reported in experiments. There is usually stress overshooting at first, and it may take up to an hour [14] to reach a steady state. We therefore resorted to a Crank-Nicolson scheme:

$$\frac{\widehat{\tau}_{n+1} - \widehat{\tau}_n}{\Delta t} = {}^1\!/_2 \left(\phi\left(\widehat{\tau}_n\right) + \phi\left(\widehat{\tau}_{n+1}\right)\right)$$

where the indices denote time: $\widehat{\tau}_n \equiv \widehat{\tau}(t = n\Delta t)$. Linearization of the above equation gives:

$$\left(\mathbf{II} - \frac{\Delta t}{2}\boldsymbol{\nabla\phi}\right) \widehat{\tau}_{n+1} = \widehat{\tau}_n + \Delta t \ \left(\phi\left(\widehat{\tau}_n\right) - {}^1\!/_2 \boldsymbol{\nabla\phi} \cdot \widehat{\tau}_n\right)$$

This process is time-iterated until convergence is reached.

2.4.5 Stress and velocity profiles

Figure 2.4.2 presents velocity and micellar shear stress profiles in the shear-banded system, approximately halfway through the plateau, and Figure 2.4.3 focuses on the interface of the velocity profile at different diffusive lengths.

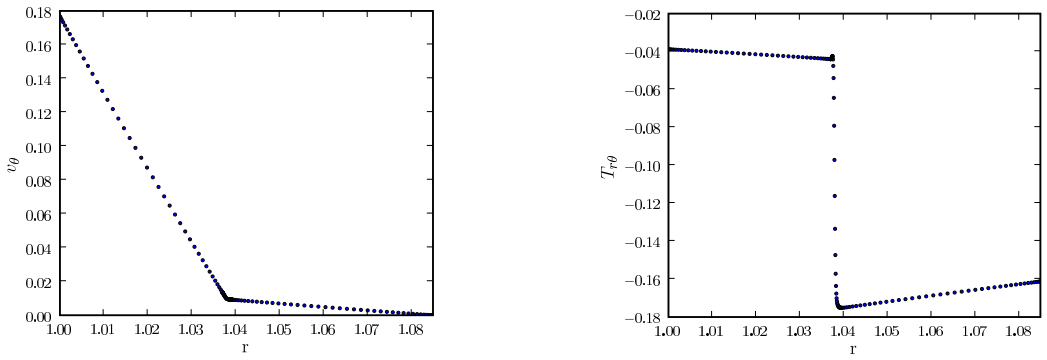

(a) Velocity profile

(b) Micellar shear stress profile

Figure 2.4.2: (a) Velocity and (b) micellar shear stress profiles at $Wi = 13.6$ and $l = 3.16 \cdot 10^{-4}$. The blue dots are the values at the collocation points.

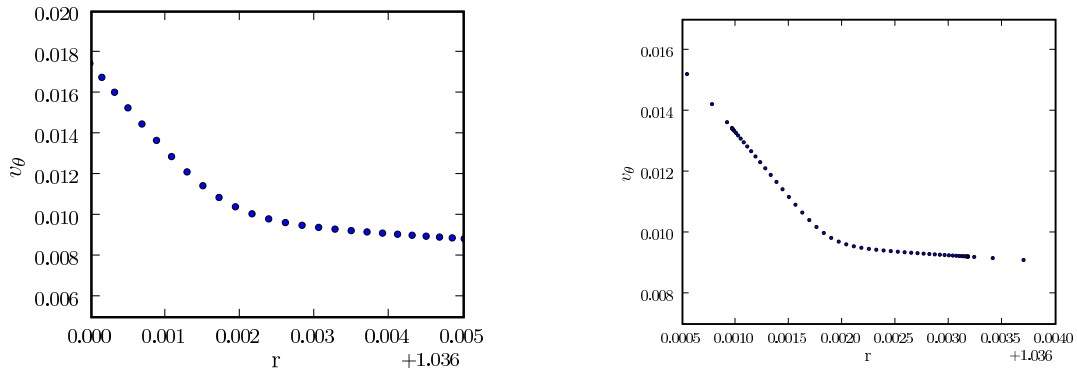

(a) $l = 10^{-3}$

(b) $l = 3.16 \cdot 10^{-4}$

Figure 2.4.3: Zoom on the interfacial region of the velocity profile at $Wi = 13.6$ for different diffusive lengths

2.4.6 Flow curve

The flow curve $\Sigma = f(\omega)$ appears in Figure 2.4.1, together with the constitutive curve and the experimental data. It may be worth noticing that both the positive-slope homogeneous branch above the stress plateau and its higher-shear rate counterpart below the plateau are stable, or at least metastable.

Chapter 3

Stability of the shear-banded flow

The Taylor-Couette shear-banded flow that was simulated in the previous part is purely azimuthal and invariant under translation along the vorticity direction. However, experiments using tracer particles [14] have provided evidence that the flow is actually three-dimensional. More recently, in 2009, Fardin *et al.* have shown the existence of Taylor-like vortices stacked along the vorticity direction and correlated with interfacial undulations [4].

We are therefore led to inquire into the stability of the purely azimuthal flow, hereafter referred to as base flow. In this chapter we first ascribe a position to our system in the stability diagram established by Fielding; thereafter we propose a fully-3D linear stability analysis of the base flow across the stress plateau, which, to the best of our knowledge, is unprecedented.

3.1 A stable system?

Let us first recall that the existence of an instability of the base flow does not imply the onset of turbulence or chaos. Consider for example the Taylor-Couette flow of a Newtonian liquid. As the applied shear rate increases, the system may display a number of stable coherent structures and patterns, including Taylor and Görtler vortices, before switching to turbulence.

Generally speaking, instability results from the bifurcation from one branch of solutions to another one. If A is an order parameter of the system, A can e.g. be zero for one type of solutions, or in other words one phase, and non-zero for another one. As shown in Figure 3.1.1, if there is an apparent jump in the order parameter at the transition, the transition involves a latent heat supply and is called subcritical[1]. Otherwise, the transition is continuous with respect to the order parameter and is called supercritical. Let us however note that the difference between the two types of transition might not be noticeable if the jump in the order parameter is small.

[1] other scenarii than the one sketched in Figure 3.1.1 are possible

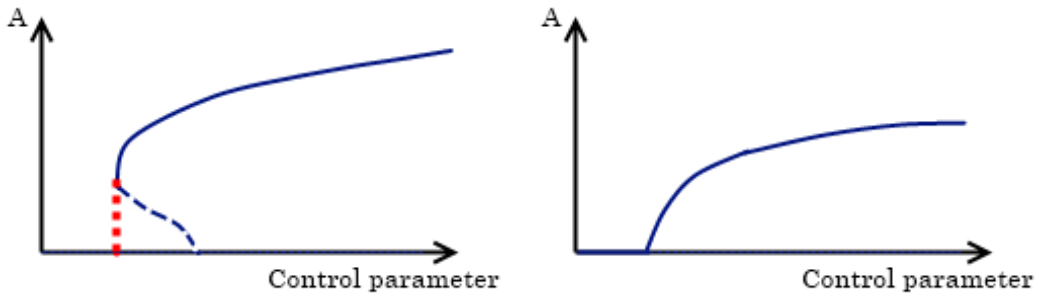

(a) Sketch of a subcritical transition (b) Sketch of a subcritical transition

Figure 3.1.1: Difference between a subcritical and a supercritical transition. A denotes an order parameter.

In the shear-banded flow of worm-like micelles, although turbulence has been observed at relatively high applied shear rates, a stable state involving vortices in the high-shear band and interface undulations has most often be reported. In a paper published in 2010 [20], Fielding studies the stability of the base flow with respect to axially-symmetric perturbations. From her results, she establishes a diagram in which the stability of a shear-banded flow depends upon the curvature of the Taylor-Couette cell and the value of the first normal-stress-difference $N_1 \propto \frac{1}{1-a}$. A rough sketch of this diagram is shown in Figure 3.1.2.

The nature of the instability will be dealt with in the next chapter. For the time being, the important point is that the model parameters we selected are located deep in the stable region of the stability diagram.

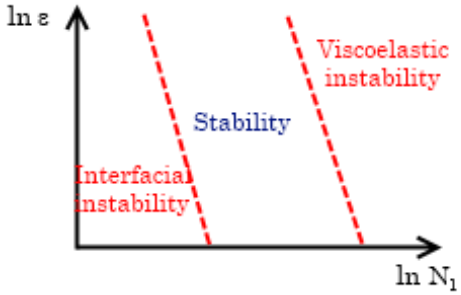

Figure 3.1.2: Rough sketch of Fielding's stability diagram[20]. $\epsilon = \frac{R_2 - R_1}{R_1}$ is a measure of the curvature of the Taylor-Couette cell. $N_1$is the first normal-stress-difference in the high-shear band

3.2 Numerical method

Notwithstanding this stability in 2D, we want to perform a 3D linear stability analysis using our multidomain grid. At least two reasons account for our determination to allow non-axisymmetric perturbations. First, non-shear banded flows of viscoelastic fluids in a Taylor-Couette geometry are

subject to instabilities that are modulated in the azimuthal direction. Second, in a previous paper investigating planar geometry [21], Fielding had found that the most unstable perturbations have a wavector in the flow direction[2].

Let us now expose the basic principle of linear stability analysis. The main idea is to linearize the equations, expand them in Fourier modes in the azimuthal and axial directions and look for perturbation eigenmodes, ie modes that are amplified exponentially, for a large set of wavenumbers *(m,k)*.

More precisely, the stress, velocity, and pressure perturbation fields are gathered in a single perturbation vector

$$\phi(r,\theta,z,t) \equiv \text{transpose}\left(\begin{array}{ccccccccc} \delta\tau_{rr} & \delta\tau_{r\theta} & \delta\tau_{rz} & \delta\tau_{\theta\theta} & \delta\tau_{\theta z} & \delta\tau_{zz} & \delta v_r & \delta v_\theta & \delta v_z & \delta p \end{array} \right)$$

Noticing that the coefficients of the DJS Eq 2.3.1 do not vary along the flow and vorticity directions, we expand the perturbation vector in Fourier series in θ and z ($c_{m,k} \in \mathbb{C}$):

$$\phi(r,\theta,z,t) = \psi(r,t) \sum_{m=0}^{\infty} \sum_{k \in 2\pi/L_z\mathbb{Z}} c_{m,k}\, e^{im\theta} e^{ikz} \tag{3.2.1}$$

The fully-3D DJS, Stokes and incompressibility equations are then linearized around the base flow profile and the perturbation $\phi(r,\theta,z,t)$ is inserted into the linearized equations. Now, if one restricts their attention to one term of the resulting sum, that is, if one selects a given wavenumber *(m,k)*, one gets a system of equations of the following form:

$$\mathcal{L}_1(\partial_t \psi) = \mathcal{L}_2(\psi, m, k) \tag{3.2.2}$$

where $\mathcal{L}_1$ and $\mathcal{L}_2$ are linear functions. In the Stokesian regime, $\mathcal{L}_1 \begin{pmatrix} \partial_t \delta\boldsymbol{\tau} \\ \partial_t \delta v \\ \partial_t \delta p \end{pmatrix} \equiv \begin{pmatrix} \partial_t \delta\boldsymbol{\tau} \\ 0 \\ 0 \end{pmatrix}$.

A Laplace transform of ψ in t gives $\psi(r,t) = \int e^{\sigma t} \psi_\sigma(r) dt$, and a discretization of space in r finally turn differential equation 3.2.2 into the following generalized eigenvalue problem, in matricial notation:

$$\sigma \mathbf{B} \widehat{\psi}_\sigma = \mathbf{A}(m,k) \widehat{\psi}_\sigma \tag{3.2.3}$$

Here, σ is a complex angular frequency, whose real part is hereafter (improperly) referred to as initial growth rate, $\mathbf{A}$ are $10\,M \times 10\,M$ matrices, with M the number of mesh points. Details of the components of $\mathbf{A}$ are provided in Appendix C.

We impose the same boundary conditions for the perturbation as for the base flow (see Chapter II), namely no slip and no stress flux on the inner and outer cylinders. No specific boundary conditions are imposed on the caps of the rheometer in the vorticity direction, which can be interpreted either as periodic boundary conditions or as an approximation of infinite cylinders. This choice is justified insofar as the cylinder length is shown to have only limited effect [20].

[2] however, she claims that this instability is cut off at the non-linear level when it reaches finite amplitude.

A Python routine can then solve Eq 3.2.3 at given *(m,k)*.

In the linear regime, an eigenmode ψ_σ associated with eigenvalue σ, arising because of noise, grows like: $\psi_\sigma(r,t) = e^{\sigma t}\psi_\sigma(r,0)$. Therefore the criterion for (asymptotic) stability is given by:

$$\boxed{\Re e(\sigma) > 0 \quad \forall \sigma \text{ satisfying (3.2.3)}, \ \forall (m,k)}$$

Due to discretization, spurious eigenvalues pop up in Eigenvalue Problem 3.2.3. To discriminate them from physical ones, the eigenvalue problem is also solved at a different spatial resolution. Spurious eigenvalues are expected to vary dramatically as the resolution changes, whereas physical ones are supposed to stay constant. We automated the discrimination process.

3.3 Results of the linear stability analysis

As expected, axisymmetric perturbations *(m,k=0)* are found to decay with time, insofar as no eigenvalue with a positive real part is detected.

However, for non-zero axial wavenumbers, we do find positive initial growth rates throughout the stress plateau. This means that the shear-banded system actually is linearly unstable.

At a given Weissenberg number[3] Wi, let us define $\sigma^\star_{m,k}$ as the physical eigenvalue solving Eq 3.2.3 for wavenumber *(m,k)* with the maximal real part: $\Re e(\sigma^\star_{m,k}) = \max \Re e(\sigma_{m,k})$, for $\sigma_{m,k}$ *in* $Sp(A(m,k)|B)$, the spectrum of eigenvalues of Eq 3.2.3. We now define $\sigma^\star$as the eigenvalue among the $\sigma^\star_{m,k}$ with the maximal real-part: $\Re e(\sigma^\star) = \sigma^\star_{m^\star,k^\star} = \max_{(m,k)} \Re e(\sigma^\star_{m,k})$.

Figure 3.3.1 shows the variation of the peak initial growth rate $\Re e(\sigma^\star)$ for Weissenberg numbers across the plateau, and for various diffusive lengths l. It proves that the full extent of the plateau is linearly unstable, that the instability decreases soon after the onset of the plateau and, finally, that the instability grows when the diffusive length decreases.

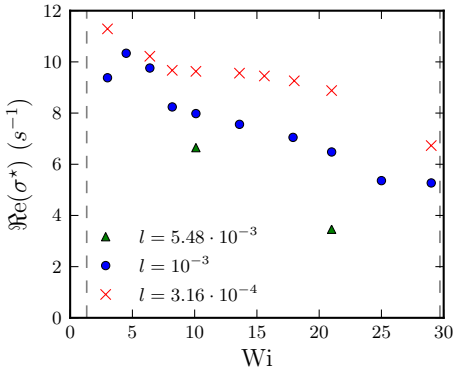

Figure 3.3.1: Variation of the peak initial growth rate $\Re e(\sigma^\star)$ across the stress plateau

[3]reminder: the Weissenberg number is here the adimensional analogue of the applied shear rate

Since both the peak axial and azimuthal wavenumbers $(k^\star, m^\star)$ are non-zero, the eigenmode is structured in spirals winding around the inner cylinder. This means that all the points on a given spiral experience the same velocity and stress fields. Figure 3.3.2 shows the points in the gap where the velocity field reaches, in norm, between 83 and 87% of its maximal value.

Those spirals have an azimuthal angular velocity $\Omega_{pert,m} = \frac{\Im m(\sigma)}{m}$. Given their finite extension, it is rather intricate to determine if this value is equal to the local velocity at the core of the perturbative vortex, even when such a vortex core can be defined. However, when the perturbation is strongly peaked at a given radial position in the gap, it seems to be the case for most, but not all, peak eigenmodes. In those cases, the cores of the perturbation is thus advected with the (base) flow. Nevertheless one must bear in mind that linear eigenmodes will interact if more than one is unstable, which is obviously the case if the peak eigenvalue is degenerate for symmetry reasons, and their initial growth rate is comparable. Moreover, non-linear effects will come into play as soon as they reach finite amplitude.

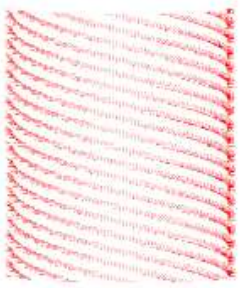

Figure 3.3.2: Points with perturbed velocity δv such that $0.83 \leqslant \frac{\|\delta v\|}{\|\delta v\|_{max}} \leqslant 0.87$ for the peak eigenmode at Wi=10.1, k=14.4, m=6

In conclusion of this chapter, we have shown that our shear-banded system becomes linearly unstable when 3D perturbations are taken into account. Yet, so far, very little has been said about the instability that sets in.

Chapter 4

Nature of the instability

We now turn to a more thorough study of the instability; in particular we endeavour to elucidate the nature of the peak instability: does it originate at the interface? or does it arise in the high-shear band?

Answering those questions is important to better understanding how a change in the parameters might affect the flow and to what extent the shear flow of a micellar solution resembles that of a polymer solution.

4.1 Two major types of instability

Two types of instability appear in the stability diagram established in [20]: at small first normal-stress-difference and relatively small curvature, the instability is interfacial; at large first normal-stress-difference in the high-shear band and/or large curvature, it is a Taylor-Couette viscoelastic instability due to the high-shear band.

4.1.1 Interfacial instability

This type of instability is notably encountered in the planar shear-banded flow of a worm-like micellar solution.

The mechanism allegedly responsible for this instability is that any deformation of the interface exposes the difference in normal stresses between the shear bands, which amplifies the deformation. Alternatively [14], given that the shear rates are different on both sides of the interface, the deformation induces a discontinuity in velocity at the interface and recirculation is needed to restore continuity.

Ref [20] shows a very good correlation between the jump ΔN_2 in the second normal-stress-difference between the shear bands and the strength of this instability (all other parameters but N_1 and a being kept equal).

However, in planar geometry, the interfacial instability decreases (after a short increase) as the interface moves towards the outer cylinder, while ΔN_2 remains constant. Naturally one could argue the change in the proportion of the shear bands, which accomodate the pertubation, and this alone, accounts for the decrease. Nonetheless this would be counterintuitive since the high-shear band is less viscous and its width increases while the instability is decreasing.

We envisage two alternative reasons, which rely much more on the limited number of variables that are modified as the applied shear rate increases than to a physical understanding:

- ⋆ the velocity at the interface decreases as the latter is shifted towards the outer wall. If for some reason a vortex is generated, the perturbative radial velocity may be coupled to the azimuthal velocity of the base flow and it will therefore decrease.
- ⋆ in order to adjust the size of the vortices to the band sizes, the wavenumber of the perturbation has to adapt and interface instability might be less acute for the new wavenumber

Finally, let us remark that interfacial instability is suppressed by curvature. A possible explanation for this is that, on top of an interface which is already quite curved, the curvature of the deformation of the interface will be less noticeable.

4.1.2 Bulk viscoelastic instability

We now turn to an instability which is purely linked with the elastic properties of the fluid. In a paper entitled "Elastic instability and Curved Streamlines" published in 1996 [22], Pakdel and McKinley made use of an analogy with inertial Görtler vortices to propose a criterion - later dubbed Pakdel-McKinley criterion [23]- that relates the onset of elastic instability to the curvature of the streamlines. This criterion can be written as follows:

$$\boxed{\frac{\mathcal{L}}{\mathcal{R}}\frac{N_1}{\sigma} \geqslant M_{crit}^2} \tag{4.1.1}$$

where M_{crit} is a constant... that actually depends on the type of the flow, the nature of the geometry and the constitutive model. σ and N_1 are as usual the polymeric shear stress and the first normal-stress-difference, $\mathcal{L} \equiv \lambda_M v$ is the characteristic distance over which perturbation relax along a streamline and $\mathcal{R}$ is some characteristic measure of the local radius of curvature. In other words, $\frac{l}{\mathcal{R}}$ is the angle seen by a polymer chain while the stress it has stored relaxes.

Although this criterion was mainly derived thanks to (non-)dimensional analysis of constitutive equations, some hints for physical interpretation were suggested. The origin of the instability lies with the coupling between radial velocity and normal stresses. Consider a radial velocity gradient perturbation in the microscopic dumbbell picture. Its effect on a given dumbbell is to move the beads further apart. Taking into account the shear base flow, the difference in their azimuthal velocity v_θ will increase too, which results in larger normal stress $\tau_{\theta\theta}$. But since the dumbbell has also been stretched in the radial direction, τ_{rr} is also larger. The natural response is that the larger τ_{rr} backfires on the radial velocity and kills the perturbation. But in curved geometry $\tau_{\theta\theta}$ also

impacts the radial velocity and amplifies the perturbation. Which of those two antagonistic effects is the greater determines whether the perturbation grows or decays.

As a matter of fact, Larson *et al.* had demonstrated the existence of purely elastic instability and proposed another version of the Pakdel-McKinley criterion in a paper published a few years before [24]. Translated into our notations, their version was: $\epsilon Wi^2 \geqslant \frac{M_{crit}^2}{2}$. Let us show that, for a Taylor-Couette flow with the inner cylinder rotating in the small-gap approximation, this earlier version is equivalent to Eq 4.1.1 if and only if the outer wall is stationary.

$$\begin{aligned}\frac{\mathcal{L}}{\mathcal{R}}\frac{N_1}{\sigma} &= \frac{\lambda_M v(R_1)}{R_1} 2\lambda_M \dot{\gamma} \\ &= 2\lambda_M^2 \dot{\gamma} \frac{v(R_1)}{d}\frac{d}{R_1} \\ &= 2\epsilon \frac{Wi}{\dot{\gamma}}\frac{v(R_1)}{d}\end{aligned}$$

where we remind that d is the gap width, $v(R_1)$ is the inner cylinder velocity and $\frac{N_1}{\sigma} = 2\lambda_M\dot{\gamma}$. This comes down to Eq 4.1.1 if and only if $v(R_1)$ is the velocity difference between the walls, ie if the outer wall is stationary.

Finally, it might be worth remarking that the Pakdel-McKinley criterion implies that adding a solid body rotation to a Taylor-Couette flow affects its stability, since it modifies the value of $\mathcal{L}$.

4.2 How to discriminate between the two types of instability?

4.2.1 Direct visualization of the eigenmodes

Direct visualization of the unstable eigenmodes may not be sufficient to determine the nature of the instability, for one may expect, even in the interfacial case, the secondary flow to be mainly localised in the high-shear band due to its lower apparent viscosity [25] whereas, on the other hand, an instability in the high-shear band could induce one in the low-shear band via the interface.

4.2.2 Variation of the diffusive length

In Ref [20] it is said that decreasing the diffusive length l dramatically enhances the interfacial instability whereas it does not affect the bulk instability. One could then think that varying l will indicate the nature of the instability.

In our simulations, all peak initial growth rates are increased when the diffusive length is decreased from 10^{-3} to $3.16 \cdot 10^{-4}$. However we claim that this discrimination method is not valid in our case, as we shall show in section 4.2.3

4.2.3 Analysis of a non-shear-banded flow that has the same features as the high-shear band

Principle

We want to determine whether a bulk viscoelastic instability of the high-shear band is possible in the system under study.

As a preliminary step, we compute criterion 4.1.1 for values of M_{crit} ranging from 1 to 8 (values which are usually encountered) evaluating the variables in the high-shear band. Depending on M_{crit}, a viscoelastic instability is predicted to set in either as soon as the high-shear band appears or at some point in the first half of the plateau, and naturally for all the higher applied shear rates.

Our aim is now to overcome the indeterminacy of M_{crit}. In order to do so, we came up with the following idea: we reproduce the characteristics of the high-shear band in a non-shear-banded flow extendng from the inner wall to a new outer wall that replaces the interface, and we study its stability. In other words, we simulate a shear flow that has exactly the same features as the high-shear band, namely the same velocity and stress profiles. This is achieved by creating a smaller gap of the width of the high-shear band, and selecting the proper angular velocities on the walls[1].

The one difference between the smaller gap flow and the high-shear band is the boundary condition at the outer wall/interface, which differs. Notwithstanding this, if the instability is a bulk viscoelastic one, we expect to observe an instability in the non-shear-banded smaller-gap flow too.

A viscoelastic instability throughout the stress plateau

Applying the smaller-gap method to various Weissenberg numbers throughout the plateau, we find that the bulk flow is unstable from the onset to the end of the plateau and the larger the Weissenberg number, the stronger the instability. This points to the existence of a viscoelastic instability of the high-shear band. However, even in case this result should be confirmed by our subsequent analysis, what matters most to us is the nature of the peak instability and one could imagine that the viscoelastic one is outshone by an even stronger instability.

Before turning to the question of the peak instability, three points are worth mentioning.

First, we have checked that the low-shear band cannot give birth to a viscoelastic instability, at least in the absence of any destabilizing factor.

Secondly, unexpectedly, we have found that the initial growth rate of a bulk perturbation in the smaller gap does actually depend on the value of the diffusive length l. Increasing l dramatically stabilizes the flow. A simple explanation accounting for this is that diffusion (whose strength is controlled by l) smoothens both velocity and stress profiles and thus opposes any sharp pertubation. In consequence, decreasing l enhances both the viscoelastic instability and the interfacial one, which

[1] The outer cylinder of the smaller gap needs to move too, because the interface moves in the shear-banded system and solid body rotation matters, as emphasized in section 4.1.2.

proves the method proposed in section 4.2.2 is not reliable here. It seems, though, that the strength of the bulk instability saturates for $l \sim 10^{-4}$ and reaches the same value as for $l = 0$ but computer constraints prevent us to proble too small interfacial widths $O(l)$ in the shear-banded system.

Thirdly, even though our JS parameter $a \simeq 0.985$ is close to unity, the instability is radically different from an Oldroyd-B one ($a = 1$). Indeed, for relatively small axial wavenumbers, a wide range of azimuthal wavenumbers m is unstable in the JS model, whereas only m of order unity are unstable in the case of an Oldroyd-B fluid.

4.3 A bulk viscoelastic instability at large Weissenberg numbers

At large Wi, close to the end of the plateau, there is very good quantitative agreement between the values of the peak eigenvalues in the shear-banded system and in the smaller-gap, which is a clear indication that the instability is of the same nature in both systems. This quantitative agreement is shown in Figure 4.3.1, where the spectrum of eigenvalues solving Eq 3.2.3 for the most unstable wavevector in the shear-banded system at $Wi = 29$ and $l = 3.16 \cdot 10^{-4}$ is superimposed with the spectra for the same problem at $l = 10^{-3}$ and for the smaller-gap system[2] ($l = 3.16 \cdot 10^{-4}$).

The contour plot in Figure 4.3.2 represents the dispersion relation $\Re e(\sigma^{\star}_{m,k}) = f(m,k)$ in the *(k,m)*-plane for the shear-banded and smaller-gap systems and demonstrates that the agreement is also satisfactory for other wavevectors, at least for $k \leqslant 40$, which points to a dominance of the bulk instability all over the *(k,m)*-plane.

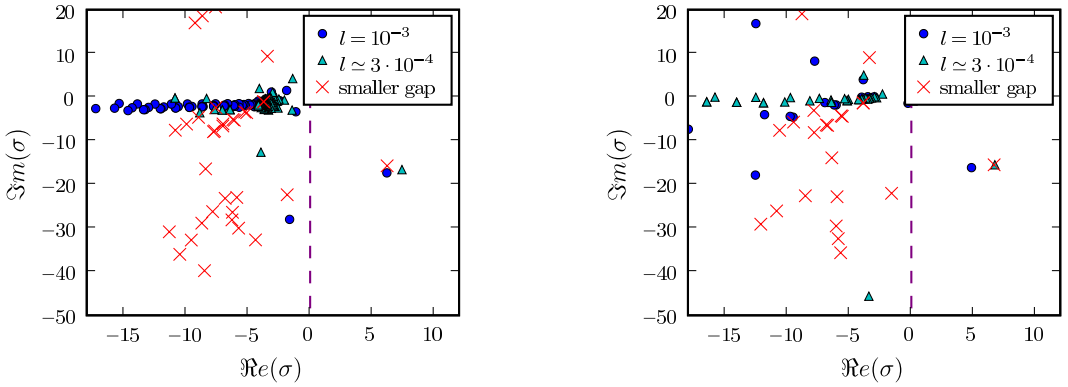

(a) $Wi = 21$,$k = 27.7$, $m = 15$

(b) $Wi = 29$,$k = 20.54$, $m = 21$

Figure 4.3.1: Eigenvalue spectra at various Wi for the shear-banded system ((•) $l = 10^{-3}$and (▲) $l = 3.16 \cdot 10^{-4}$) and the smaller-gap flow (×)

[2] the variables have naturally been properly rescaled to allow comparison

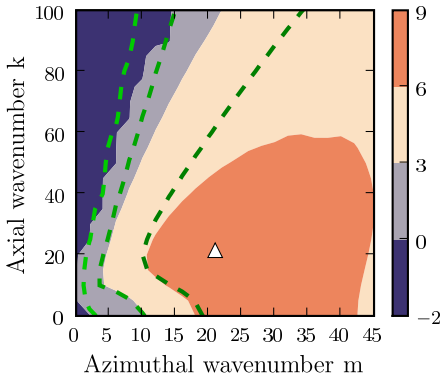

Figure 4.3.2: Contour plots representing the dispersion relation $\Re e(\sigma^{\star}_{m,k}) = f(m,k)$ at Wi=29, $l = 3.16 \cdot 10^{-4}$(filled regions). The green dashed lines represent the contours for the corresponding smaller-gap system. $\triangle$: the peak wavenumber $(k^{\star}, m^{\star})$ in the shear-banded system.

As a further argument in favour of a bulk instability of the high-shear band, the peak eigenfunctions in the smaller-gap, homogeneous flow and in the widely dominant (at large Wi) high-shear band look very much alike[3] , as can be seen in Figure 4.3.3. The depicted eigenmode δv is real; it has been obtained from the real part of the complex eigenfunction[4] at t=0:

$$\begin{aligned} \delta v &= \Re e(\underline{\delta v}\, e^{i(kz+m\theta)}) \\ &= \Re e(\underline{\delta v})\, \cos(kz+m\theta) - \Im m(\underline{\delta v})\, \sin(kz+m\theta) \end{aligned}$$

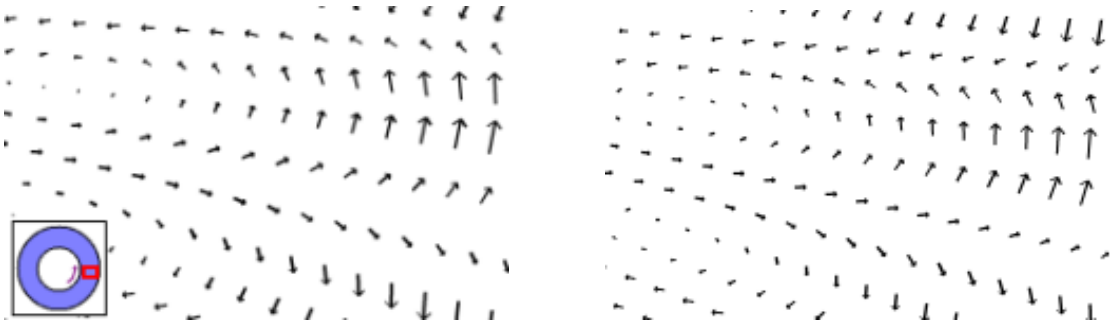

(a) Shear-banded system (zoom) (b) Smaller gap (zoom)

Figure 4.3.3: View from the top of the velocity profile (zoom) of (a) the most unstable eigenmode in the shear-banded system at $Wi = 29$ ($k = 20.54,\ m = 21$). There is no perturbative velocity field in the low-shear band (out of focus)(b) the same region of the corresponding smaller gap flow

[3] We have found no explanation as for the reason why the vortices should be close to the interface/outer wall and not in the vicinity of the inner cylinder, where curvature and velocity are larger.

[4] this comes from the Fourier decomposition of the perturbation. Given the initial function is real, $c_{-m,-k} = c^{*}_{m,k}$ using the notations of Eq 3.2.1

4.4 An instability strongly coupled with the interface at small Weissenberg numbers

Contrariwise, at small Wi, near the onset of the plateau, the peak instability occurs at lower, almost constant axial wavenumber ($k^\star \approx 15$). After a swift shift to smaller azimuthal wavenumbers (from $m^\star = 30$ to $m^\star = 9$ between $Wi = 3.0$ and $Wi \simeq 6$), the azimuthal wavenumber tends to be remain constant too, and, consequently, the most unstable region is pinned at some value in the (k, m)-plane.

Unlike the situation described in section 4.3, the peak eigenvalues $\sigma^\star_{m,k}$ in the shear-banded systems are here much larger than their counterparts in the smaller gap flow. While some secondary eigenvalues in the former system can be matched with eigenvalues observed in the latter system, there is no matching for the peak ones. Finally, the most unstable eigenmode is peaked at the interface and pressure is locally altered there. The vortices appear to be localised in the low-shear band when it is widely dominant, but, as already mentioned, we have checked that the isolated bulk flow in that band is linearly stable.

Those arguments are all in favour of an interfacial instability, or, more rigorously, an instability in which the interface plays a major role.

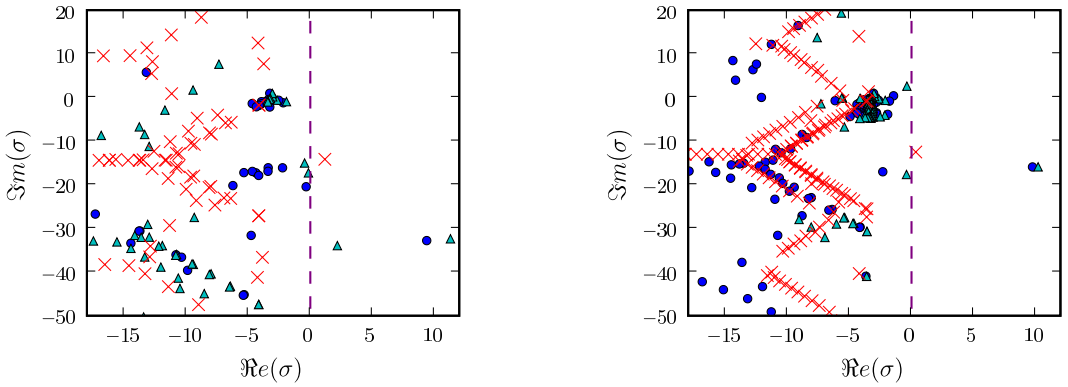

(a) $Wi = 3.0$, $k = 14.4$, $m = 30$ (b) $Wi = 6.4$, $k = 14.4$, $m = 9$

Figure 4.4.1: Superimposed spectra for the shear-banded system and the smaller gap one at various Wi (peak wavevector for $l = 3.16 \cdot 10^{-4}$). Refer to Figure 4.4.1 for the legend.

Let us now consider the dispersion relations $\mathcal{R}e(\sigma) = f(m, k)$ (Figure 4.4.2). It is worth remarking that their global shape is reminiscent of the dispersion relations found by Fielding [**?**] in the planar case, especially for $Wi = 3$. That similarity is in accordance with the small curvature $\epsilon \ll 1$ of the viscometer. The very wide range of unstable wavevectors is nonetheless puzzling in comparison with the laminar flow reported for those applied shear rates. The depiction of the peak eigenmode at Wi=3.0 in Figure 4.4.3 indicates that the perturbative velocity in the vorticity direction is maximal close to the interface (Subfigure b).

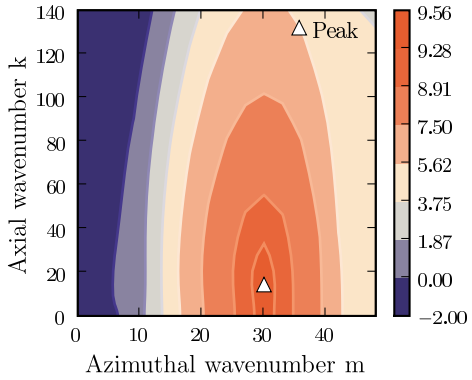

Figure 4.4.2: Filled contour plot of the dispersion relation $\Re e(\sigma^{\star}_{m,k}) = f(m,k)$ at Wi=3.0 for $l = 10^{-3}$

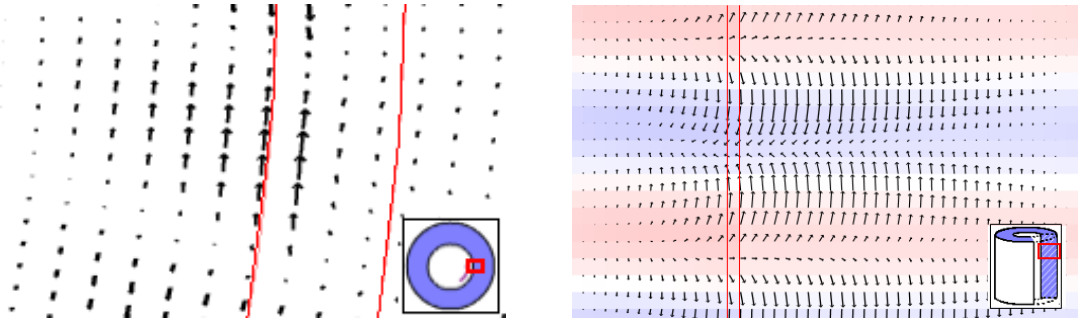

(a) (b)

Figure 4.4.3: (a) View from the top and (b) cross section of the velocity field for the peak eigenfunction at $Wi = 3.0,\ l = 3.16 \cdot 10^{-4}$ ($k^{\star} = 14.37,\ m^{\star} = 30$). Colours represent pressure p, blue denoting lower values and red higher values.

4.5 A change of eigenvalue in-between

In-between those two extremities of the plateau, the "interfacial" instability that prevails at low Wi seems to weaken when the Weissenberg number grows. This had also been observed in the planar case, as we have discussed in section 4.1.1.

In parallel, a second region of locally maximal instability emerges in the *(k,m)*-plane, at larger values of the axial and azimuthal wavenumbers (see Figure 4.5.2).

In this second region, the peak eigenvalues are not quantitatively reproduced by smaller gap simulations either. However, one can rather satisfactorily associate them individually with eigenvalues in the smaller gap flow. We defend the idea that those eigenmodes originate in a bulk instability in the high-shear band, but get somehow coupled with the interface. Secondary flow is then induced in the low-shear band via the interface. Recirculation in the low-shear band would then account for the eigenvalue discrepancy between the shear-banded system and the smaller gap simulations. As

expected, the discrepancies get lower and lower as Wi increases, in other words as the proportion of the low-shear band decreases. Figure 4.5.1 shows cross-sections of the most unstable eigenmodes for both of these regions. The reader might find it instructive to compare them with the eigenmode at Wi=3.0 depicted in Figure 4.4.3.

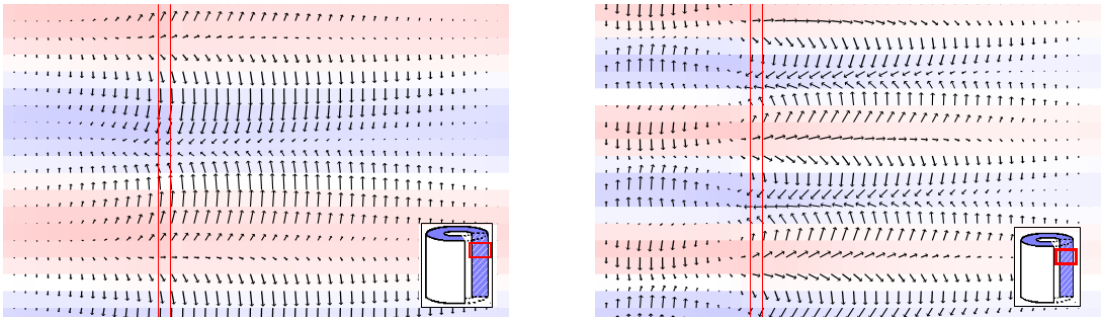

(a) (b)

Figure 4.5.1: Side views of the most unstable eigenmodes at $Wi = 10.1$, $l = 3.16 \cdot 10^{-4}$ for the following wavevectors: (a) k=14.4, m=6 (first region), (b) k=25 m=24 (second region). The red lines are the boundaries of our central domain, which comprises the interface

At some Weissenberg number Wi_c the second very unstable region overtakes that which was dominant so far, thereby inducing a jump in the axial wavernumber of the peak eigenmode to larger values. Simultaneously, spectra at various wavenumbers throughout the *(k,m)*-plane indicate a change in the peak eigenvalue: this means that the new type of instability overruns the whole *(k,m)*-plane, and the peak corresponding to "interfacial" instability can no longer be distinguished in a contour plot of the disperion relation. Let us also remark that the critical Weissenberg number Wi_c depends upon the diffusive length l. At $l = 10^{-3}$, Wi_c is around 10, whereas it is comprised between 6 and 8 at $l = 3.16 \cdot 10^{-4}$. For Wi between those two critical W_c, the second type of instability (originally bulk viscoelastic in our claim) is more enhanced than the first type (interface-connected) when l decreases from 10^{-3} to $3.16 \cdot 10^{-4}$.

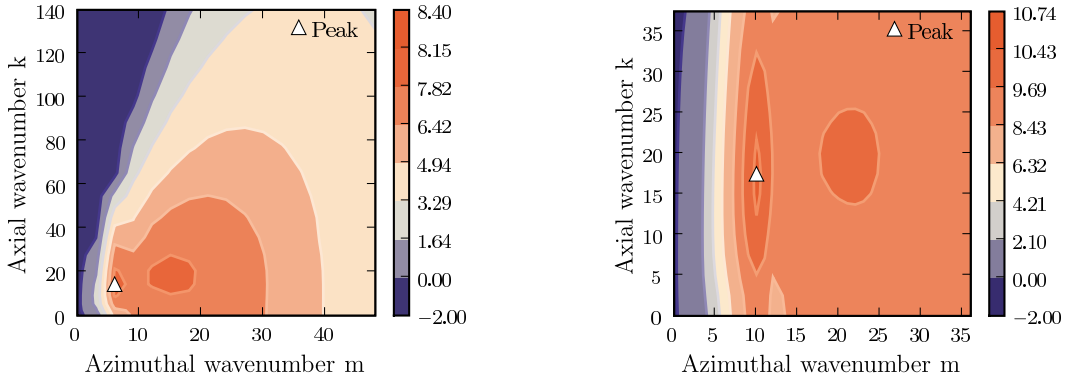

(a) $Wi = 8.2$, $l = 10^{-3}$ (b) $Wi = 6.4$, $l = 3.16 \cdot 10^{-4}$ (Zoom)

Figure 4.5.2: Contour plots of the dispersion relation, featuring two competing unstable regions

After studying the dominant instabilities predicted by our simulations, we now want to test our results against experimental data.

4.6 Comparison with experimental data

The order of magnitude of the axial wavenumber experimentally observed agrees with the peak one in our simulations, insofar as both are millimetric.

However, S. Lerouge and co-workers [3] reported a continuous decrease of the axial wavenumber k with Wi, whereas our simulations would rather indicate a jump to higher values of k when the instability switches to a viscoelastic bulk instability, and a decrease of k only at the end of the plateau.

Beside the reserves one may express regarding the fitting of model parameters and the admitted difficulty inherent to experimental measurements near the onset of the plateau (due to the small proportion of the high-shear band), it is worth remarking that, near the onset of the plateau, the steady-state wavelength is observed only after a transient. The initial axial wavenumber is said to be down to twice smaller than the steady-state one. Therefore, it is much closer to our peak "interfacial" axial wavenumber. Moreover, the ratio of the peak wavenumbers for "bulk" instabilities "interfacial" in our simulations is also very roughly 2 at the switch between the two instabilities. We may therefore propose a scenario in which an initial interfacial instability is replaced by another type of instability, possibly bulk, of shorter wavelength. Still, the wavenumbers observed experimentally remain larger than those obtained in our simulations for relatively small applied shear rates, by a factor of approximately 2.

Besides, the existence of vortices in the high-shear band could explain the failure of birefringence experiments to observe strong orientation of the micelles in this band.

Chapter 5

Alternative approaches to the study of the shear-banded flow

In the last few chapters we have relied on a traditional Johnson-Segalman model to simulate the base flow and analyse its stability. This approach has been successful insofar as we have been able to exhibit a linear instability for model parameters fitting experimental data reasonably well.

However, only little physics is involved in the Johnson-Segalman model, and it might be desirable to have a larger range of parameters to adjust in the shear-banded system so as to better understand e.g. the respective roles of the first and second normal-stress-differences. In so doing, concentration discrepancies between the bands could also be taken into account. Moreover experimental observation of severe breach[1] of the lever rule in Taylor-Couette has been reported, which requires to be able to arbitrarily select the position of the interface in our simulation.

Contrary to the previous chapters which presented finished work, this section rather aims at giving an outline of two alternative approaches, the second of which is an ongoing undertaking.

5.1 Lattice Boltzmann Method

Relying on the results of our pseudospectral simulations, we wanted to test the validity of a pre-existing lattice Boltzmann code adapted to the Johnson-Segalman model, written by Marenducci and Morozov. In this code, the lattice Boltzmann method is used in order to solve the (sole) Navier-Stokes equations.

This computational fluid dynamics method is generally used to model Newtonian fluids. Very roughly, its principle consists in simulating the motion of fictitious particles over a discrete lattice mesh. Particles can propagate between meshes and collision processes obey the Boltzmann equation,

[1] less severe breach of the lever rule has also been reported in some papers [3], but we personally think this apparent breach only stems from the neglect of shear rate non-uniformity due to curvature by the authors

ie the collision probability is proportional to the variation of the local density compared to its equilibrium value.

The troubleshooting test showed that the Lattice Boltzmann code did not give the expected results. This marked the end of the first attempt to find an alternative approach.

5.2 Split fluid

We now set aside the idea to model the whole shear-banded system with a single constutive equation. Instead, each band shall obey a specifically-tailored constitutive model. The shear-banded system will then consist of the juxtaposition of those two bands, separated by an interface with a surface tension - if needed - but zero width. Consequently the position of the interface can be arbitrarily fixed and rheological properties of one band can be adjusted without affecting the other one.

5.2.1 Fitting model parameters

The crucial step in this approach is to determine the model parameters we want to impose. Indeed, our objective is to have a large enough set of parameters to fit experimental data and to control some extra parameters, but, on the other hand, we cannot manage too many free parameters in our simulations.

Hereafter index **I** will refer to the low-shear band and index **II** will refer to the high-shear band.

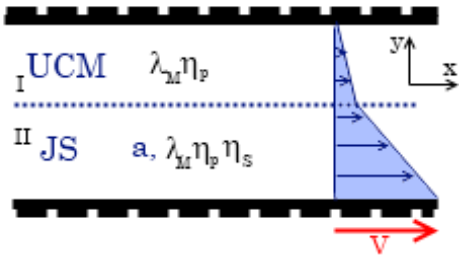

Figure 5.2.1: Sketch of the split fluid

Fluid I Experimental measurements on a worm-like micellar solution indicate that, at low applied shear rates ω, the total shear stress and the first-normal stress difference are correctly modelled by an Upper Convected Maxwell (UCM) fluid, ie they obey the following scalings:

$$\Sigma \sim \dot{\gamma}$$

$$N_1 \sim \dot{\gamma}^2$$

This is more arguable just below the onset of the plateau. However, for the sake of simplicity, the low-shear band shall be modelled as a UCM fluid. Two parameters will thus need to be determined:

- ⋆ the relaxation time λ_M^I
- ⋆ the polymeric/micellar viscosity η_p^I

Fluid II We suspect the fluid dynamics in fluid II to be more complex than in fluid I, so we shall make use of more model parameters. Since we want to control the second normal-stress-difference ΔN_2 and $\Delta N_2 = 0$ in an Oldroyd-B fluid, we resort to a diffusionless Johnson-Segalman model. Besides, we do not want the total shear stress to decay to 0 as $\dot{\gamma} \to \infty$, so a non-zero solvent viscosity will be needed.

Fluid II will thus be be characterized by four parameters:

- ⋆ its relaxation time λ_M^{II}
- ⋆ the JS parameter a
- ⋆ the polymeric/micellar viscosity η_p^{II}
- ⋆ the solvent viscosity η_s^{II}

To this list must naturally be added the interfacial tension Γ.

Fitting parameters with experimental data The experimental data we use consist of a flow curve $\Sigma = f(\omega)$ and a measurement of N_1as a function of the applied shear rate $N_1 = f(\omega)$.

Those curves enable us to determine: the high and low shear rates $\dot{\gamma}_H$ and $\dot{\gamma}_l$, and fluid I parameters λ_M^I and η_p^I , as well as the total shear stress Σ_p on the plateau. For reasons detailed in Chapter VI, we prefer not to use normal stress measurements on the plateau.

For every point on the plateau, the other model parameters result from the arbitrary selection of the following control parameters: the value N_{1H} of N_1 in the high-shear band, the viscosity ratio $\beta \equiv \frac{\eta_s}{\eta_p}$ and the second normal-stress-difference $\Delta N_2 = N_{2H}$. In fact, there are some constraints on the choice of the third control parameter if the first two are fixed. Say for instance N_{1H} and N_2 are fixed. Then, for a JS model in general, $\frac{\Sigma_p}{N_1} = P_{N_2}(\lambda_M)$, where P_{N_2} is a second-order polynomial. Assuming $\beta \ll 1$ and $N_2 < 0$, the existence of real roots requires

$$\beta \leqslant \frac{\Sigma_{xy}^2}{4|N_2|(N_1 - |N_2|)}$$

5.2.2 Linear analysis for a plane Couette flow

In plane Couette geometry, the shear rate and the stresses are uniform in each band, so the base flow can easily be solved analytically.

The same equations as in our previous approach in Part IV apply for the bulk flow within each band, but here extra boundary conditions must be implemented at the interface. Moreover this interface can be deformed around its base position h, so its position at time t is:

$$h'(t) = h + \delta h(t)$$

Here, the primes denote the perturbed quantity, the variables alone correspond to the base flow values and the δ denote the perturbation. For a given quantity Q, let us also define$\Delta[Q]$ as the jump of Q across the interface: $\Delta[Q] \equiv Q^{II} - Q^{I}$. Using first-order expansions and neglecting higher-order terms, one obtains the following boundary conditions:

- ⋆ for the continuity of tangential velocities at the interface: $\delta v_z^I = \delta v_z^{II}$ and $\Delta[\delta v_x + D_y v_x \cdot h] = 0$
- ⋆ for the impermeability condition of the material interface $v'^I \cdot \underline{n} = v'^{II} \cdot \underline{n} = V \cdot \underline{n}$, where n is the normal to the interface, and the continuity of the normal velocity: $-v_x^I \partial_x h + \delta v_y^I = \frac{\partial \delta h}{\partial t}$ and $\delta v_y^I = \delta v_y^{II}$
- ⋆ for the projection on the x axis of the stress balance $\Delta[\underline{\underline{\Sigma}} \cdot \underline{n}] = \Gamma \kappa \underline{n}$, where κ is the curvature: $\eta_s(\partial_x \delta v_y^{II} + \partial_y \delta v_x^{II}) + \Delta[\delta T_{xy} + \partial_x h \cdot (p - T_{xx})] = 0$
- ⋆ for its projection along y: $\partial_x h \cdot \eta_s D_y v_x^{II} + 2\,\eta_s \partial_y \delta v_y^{II} + \Delta[\delta T_{yy} - \delta p] = (\frac{\partial^2 h}{\partial x^2} + \frac{\partial^2 h}{\partial z^2})\Gamma$
- ⋆ for its projection along z: $\partial_z h \cdot \Delta[p] + \Delta[\delta T_{yz} + \eta_s(\partial_y \delta v_z + \partial_z \delta v_y] = 0$

The code for the stability analysis then bears strong resemblance with the former one, except that δh has to be included in the perturbation vector

$$\phi(r, \theta, z, t) \equiv \text{transpose}\left(\begin{array}{cccccccccccc} \delta\tau_{xx} & \delta\tau_{xy} & \delta\tau_{xz} & \delta\tau_{yy} & \delta\tau_{yz} & \delta\tau_{zz} & \delta v_x & \delta v_y & \delta v_z & \delta p & \delta h \end{array} \right)$$

and model parameters are space-dependent[2].

5.2.3 Base flow and linear stability analysis for a Taylor-Couette flow

The difficulty that arises when moving to curved geometry is that no analytical velocity profile is known for the base Taylor-Couette flow of a JS fluid.

For UCM fluid I, the velocity profile is known analytically; it is the same as for a Newtonian fluid, ie

$$v^I(r) = \zeta\, r + \frac{\xi}{r}$$

[2]to solve their spatial dependence, they are simply handled like variables, that is, they are inserted in vectors such as $\left(\begin{array}{cccc} \lambda_M^I & \dots & \lambda_M^I & \lambda_M^{II} \quad \dots \quad \lambda_M^{II} \end{array} \right)$

where ζ and ξ are constants determined by the rheometer geometry and the boundary conditions on velocity.

The UCM flow is therefore solved analytically, and a boundary condition on the velocity at the interface is deduced from this solution. Noting that that high shear rate $\dot{\gamma}_H$ is to be imposed at the interface, because it results from the local stationarity condition detailed in Part II, we can now simulate the flow for the JS fluid.

The linear stability analysis is similar to that exposed for the planar case in section 5.2.2, with bulk equations adapted to curved geometry. The boundary conditions, which are slightly different, are exposed in Appendix D.

5.2.4 Results

At the present time, the code has been checked for the planar case, but simulations have not been undertaken yet. This work shall be carried on in the near future.

Chapter 6

Concerns about experimental measurements

In the course of our work we have had to fit experimental measurements of the first normal-stress-difference N_1 in a cone-and-plate rheometer in order to determine model parameters. However such a measurement is not straightforward when the flow is shear banded. To understand the problem, suppose measurements are performed on the plate of the rheometer. One could think the value of N_1 indicated by the rheometer will then be a local measurement near the plate, so it would depend on which shear band is in contact with the bottom plate! All this actually shows is that it might be worth having a closer look at the theory of normal-stress measurements.

To conclude this experimental section, we relate a short-lived experiment aimed at observing shear-banding and measuring normal stresses.

6.1 Viscometric flow in a cone-and-plate rheometer

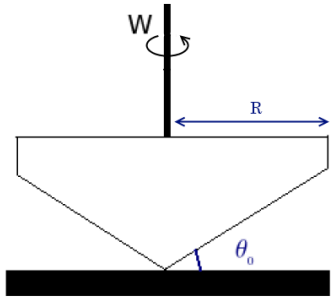

Figure 6.1.1: Viscometric flow in a cone-and-plate rheometer

The ideal planar geometry we have used in our simulations, that is, two infinite parallel plates among which one is translated at constant velocity, is not adapted to experiments, because no one has ever succeeded in constructing an infinite plate! However a small-angle cone-and-plate rheometer is similar to that ideal geometry in some respects, insofar as curvature effects are under control and the shear rate is uniform in the gap for a visometric flow.

We adopt the following notations: θ_0 is the (small) cone angle, R the radius of the plate, W the applied angular velocity of the cone (see Figure 6.1.1). r indicates the distance to the vertical axis of symmetry (neutral direction), θ the latitude (velocity gradient direction) and ϕ the longitude (velocity direction).

In the small angle limit $\theta_0 \ll 1$, at a distance r from the axis, the velocity on the cone is Wr and the gap width is $r\theta_0$, so, for a homogeneous azimuthal flow, the local shear rate $\dot{\gamma}$ is uniform across the gap: $\dot{\gamma} = \frac{W}{\theta_0}$.

Given the symmetries, the Stokesian equation of motion reads:

$$0 = -\partial_r p - \frac{1}{r^2}\partial_r(r^2 T_{rr}) + \frac{T_{\theta\theta} + T_{\phi\phi}}{r} \tag{6.1.1}$$

The polymeric stress tensor $\boldsymbol{\tau}$ is a function of $\dot{\gamma}$ only (if non-local terms are omitted), so $\partial_r T_{\theta\theta} = \partial_r \tau_{\theta\theta} + \partial_r p = \partial_r p$. Thus Eq 6.1.1 turns into:

$$\boxed{\partial_r T_{\theta\theta} = \frac{T_{\phi\phi} + T_{\theta\theta} - 2T_{rr}}{r} = \frac{N_1 + 2N_2}{r}} \tag{6.1.2}$$

The second normal stress difference $N_2(\dot{\gamma})$ is also constant, let us then evaluate it at the fluid-air interface yields: $N_2 = T_{\theta\theta}(R) - (-p_{Laplace})$, where both the ambiant pressure and the Laplace pressure are included in $p_{Laplace}$.

The integration of Eq 6.1.2 from R to r therefore yields: $T_{\theta\theta}(r) = (N_2 - p_{Laplace}) + (N_1 + 2N_2)\, ln(\frac{r}{R})$

We can now assess the total thrust $\mathcal{T}$ on the plate by integrating the normal stress: $\mathcal{T}(W) = 2\pi \int_0^R r\, T_{\theta\theta}(r)\, dr + t_{rim}$, where t_{rim} is line tension at the rim. After subtraction of the thrust at rest, so as to remove[1] $p_{Laplace}$, one gets:

$$\boxed{N_1 = \frac{2|\mathcal{T}(W) - \mathcal{T}(0)|}{\pi R^2}} \tag{6.1.3}$$

From the measurement of the total thrust on the plate, one can thus deduce the first normal-stress-difference.

At this point, it is important to note that the total thrust is the same on the plate and on the cone, for the fluid volume does not experience any variation of momentum in the axial direction so the outer forces are balanced. Consequently, in some rheometers the thrust is measured on the cone instead of the plate

[1] here, we assume the rim is not deformed by the flow

6.2 Shear-banded flow

Let us first insist on the problem. The thrust is measured locally either on the cone or on the plate, that is, either in the high-shear band or in the low-shear band. However the above reasoning showing the equality of the thrusts thus measured is still applicable. Therefore although the thrust is measured locally it has to take into account the global volume of the fluid.

6.2.1 Ideal picture

First, consider the ideal shear-banding case represented in Figure 6.2.1a, where the flow is purely azimuthal.

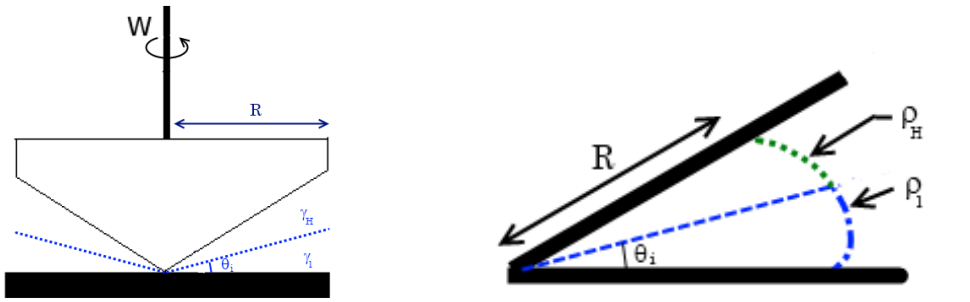

(a) Side view (b) Smooth connection of the shear-band menisci

Figure 6.2.1: Ideal shear-banded flow in a cone-and-plate rheometer

The only way the bottom shear-band may take into account the existence of the top one is through pressure. We are therefore led to examine boundary conditions on the pressure, in particular at the meniscus between the fluid and the atmosphere. Assume the radii of curvature of the meniscus are constant for each shear band, let us call them ρ_H and ρ_l. Forcing the meniscus to adjust to a given contact angle θ_Y at the solid-liquid-air interface on the plates and excluding the possibility of a kink at the junction the two menisci is sufficient to determine the radii of curvature.

Mike Cates then showed that the measured thrust obeys a lever rule:

$$|\mathcal{T}(W)| = \frac{\pi R^2}{2\theta_0}\left(\theta_i N_{1l} + (\theta_0 - \theta_i)N_{1H}\right) + f(R, \theta_Y, \gamma, p_{atm}) \tag{6.2.1}$$

where N_{1l} and N_{1H} are the respective first normal-stress-differences in the bottom and in the top shear band, p_{atm} is the atmospheric pressure and f is a function that depends only on its explicit arguments.

We propose a quick outine of this demonstration.The reader is referred to Figure 6.2.1b and to section 6.1 for the notations. In the small angle limit the distance R between the rim and the axis is the same on the cone and the plate. As shown in section 6.1, one can equate the thrust on the cone to the thrust on the plate:

$$\begin{aligned} \mathcal{T}_H &= \mathcal{T}_l \\ -\frac{\pi R^2 N_{1H}}{2} - \pi R^2 p_{Laplace\,H} + t_{rim} &= -\frac{\pi R^2 N_{1l}}{2} - \pi R^2 p_{Laplace\,l} + t_{rim} \end{aligned}$$

Here, we have used Eq 6.1.3 and expressions above. But $p_{Laplace} = \gamma\left(\frac{1}{\rho} + \frac{1}{R}\right) + p_{atm}$, so

$$N_{1H} + 2\frac{\gamma}{\rho_H} = N_{1l} + 2\frac{\gamma}{\rho_l}$$

This helps us express $\rho_H^{-1} - \rho_l^{-1}$ in terms of the rheological properties of the fluid. But we already have another expression for this difference coming from the aforementioned geometric constraints. After a few algebraic manipulations, we then find the lever rule as expressed in Eq 6.2.1.

6.2.2 Physical relevance of the ideal picture

A lever rule is thus recovered in the ideal picture depicted in Figure 6.2.1a. But is this ideal case physically relevant?

Let us recall Eq 6.1.2: $\partial_r T_{\theta\theta} = \frac{N_1+2N_2}{r}$. At the interface, the value of the right-hand term depends on the side of the interface on which one sits. As a result, $\partial_r T_{\theta\theta}$ takes different values across the interface, and so does therefore $T_{\theta\theta}$. Yet, $T_{\theta\theta}$ is the a normal stress and has to be continuous over a flat interface. This obviously leads to a contradiction. The ideal picture is not physical.

Still, one could hope the real flow will only be a perturbation of this ideal case, so that at lowest order the lever rule will still be correct. Then, it implies a bend of the interface, or rather a wavy interface because a simple bend of the interface would be at most of the order of the small cone angle, and/or a secondary flow. Kumar and Larson undertook an analytical and numerical simulation of the perturbative flow using a two-banded or three-banded gap as the base state [25]. They observed recirculation, mainly localized in the less viscous shear-band, but they did not study its impact on the thrust on the plate.

Otherwise, the geometry of the shear-bands might be quite different from that considered so far. In effect, experimental observations report the existence of a triangle-shaped high-shear band in the centre of the cone-and-plate gap, sandwiched between two low-shear bands. Images can be found in Ref [16].

6.3 Experiment

To conclude this section, I deem it appropriate to mention a one-day experiment conducted by Rut Besseling that I participated in, even though it turned out to be unsuccessful.

6.3.1 Experimental setup

Our main objective was to observe shear-banding in a particular cone-and-plate rheometer equipped with a microscope that allows direct observation of tracer particles through the (transparent) bottom plate. The small cone angle of this rheometer measures 1°.

We used a water-based solution composed of 0.3 mol/kg of $CTAB$ and 0.405 mol/kg of sodium nitrate $NaNO_3$ as salt.

0.01% in volume of tracer particles, namely surfactant-free fluorescent melamine beads of approximately 2μm of diameter, were injected into the solution. Given their size and their small concentration, we did not expect them to perturb the flow significantly.

6.3.2 Results

Our first observation was that tracer particles tended to aggregate, forming some kind of colloidal gel. A typical example of such an aggregate is shown in Figure 6.3.1 (a). After some time at higher shear rate, those aggregates tend to dissociate (Figure 6.3.1 (b))

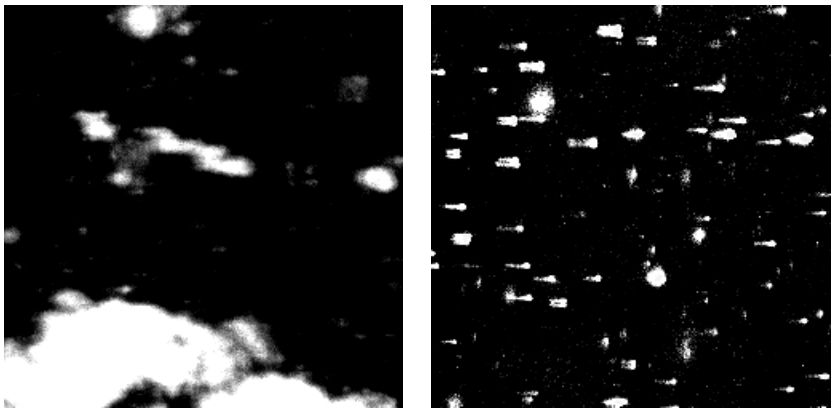

(a) Low shear rate (b) After some time at high shear rate

Figure 6.3.1: Fluorescent tracer particles under shear in a cone-and-plate rheometer. View of a cross-section parallel to the plate, observed from the bottom

However measurement of the velocities of the free tracer particles on various layers across the gap revealed the existence of very large wall-slip on the cone as well as on the plate. This was expected for the glass plate, but it is slightly more surprizing for the cone. It follows from this large wall-slip that the shear rate experienced by the fluid is much lower than the applied shear rate, hence our inability to observe shear-banding and test the results of our simulations.

Summary and Outlook

In conclusion, we have implemented a code that allows us to find the base shear-banded flow with fine resolution of the interface between the shear-bands. We have then performed a 3D linear stability analysis of the base flow and found it to be unstable, whereas the model parameters we have selected to fit experimental data belong to a stable region when only 2D perturbations are considered. Ample evidence for a bulk instability nature near the end of the stress plateau has been provided; close to its onset, on the other hand, the instability appears to be of a different type and we have observed a change of the most unstable eigenvalue at some critical Weissenberg number. Another approach, in which each shear band is modelled as a distinct fluid, has then been suggested.

Although we have tried to compare our results with experimental measurements, such a comparison will convincing only after the non-linear evolution of the perturbation has been analysed. Notwithstanding the positive amazement arising from the ability to capture non-trivial phenomena with a model involving as little physics at the microscopic scale as Johnson-Segalman, it would certainly be desirable to put forward a more sophisticated macroscopic model - one that would be simple enough, though, to allow simulations. Indeed, the phenomenology of shear-banding in worm-like micelles is much richer than what our numerical simulations show; for instance, the extra slope, ie beside curvature effects, and the kink [3] in the plateau region of the flow curve lie beyond the explanatory potential of the JS model. In the last 25 years, worm-like micelles have proved to be fraught with complex and interesting physics, but more is probably to be unearthed.

Personal appraisal

This internship has allowed me for the first time to work on a long-run scientific project, in a field that I found to be quite broad and at the intersection of many disciplines : statistical physics, rheology of viscoelastic fluids, chemistry and applied mathematics. I quite enjoyed getting an overview of those various aspects. But most of all, even though the scientific aim had been clearly set by my supervisor, I really appreciated the autonomy and the freedom he granted me in my work, thanks to which I got really involved in the project. This personal, subjective side certainly contributed to the strong will I had to elucidate unclear points and the great excitement I felt at some moments when better understanding was dawning on me. Of course, there was also the seamy side associated with this kind of scientific projects, and it was a rather dreary time that I spent, alone or with my supervisor, debugging computer code or struggling to run simulations, but, most of the time, the enthusiasm for the project outshone those darker sides.

I also relished being given the opportunity to discuss openly and argue on virtually all aspects of the projects, whether it be numerical methods or the interpretation of results. Thus, I learned that it is not sufficient that an idea or a theory be elegant and capable of explaining some elements for this idea to prove true. I was also taught to yield less easily to the tentation to content myself with the first satisfactory argument, but instead to test the hypothesis thoroughly - and maybe all the more thoroughly as we are convinced of it. Indeed, it is often much more difficult to convince somebody else than to convince onelf.

Writing an article was also quite instructive, insofar as it turned out to be more demanding and much more time-consuming than I expected.

Finally, the academic environment at the University was valuable: conferences, theory clubs, ... help broaden one's knowledge and "zoom out". I am also grateful to my supervisor for allowing me to attend the one-week scientific workshop he had organised on coherent structures and instabilities in viscoelastic flows, in Leiden.

Acknowledgments

I am very grateful to my supervisor, Alexander Morozov, for his faultless availability, the enthusiasm he has managed to sparkle when I expressed doubts about the project and the long and often fruitful discussions we have had. I also thank him for bearing my impatience when checking codes on the computer.

I thank Marc Fardin for the helpful discussions we had in Leiden, with Christopher Pipe, and the exhaustivity of his answers to my email enquiries. I am also indebted to Mike Cates for the intense discussions we had about the measurement of the first normal-stress-difference and for accepting me in his Department, to Davide Marenduzzo for the lattice Boltzmann code he had written with Alexander and to Rut Besseling for giving me a foretaste of experimental rheology.

Finally, I thank Sandra Lerouge for allowing me to use her experimental measurements.

Notations

Symbol	Definition
$\dot{\gamma}$	local shear rate
ω	applied shear rate
σ	polymeric/micellar shear stress
Σ	total shear stress
$\boldsymbol{\tau}$	polymeric/micellar stress tensor
$\mathbf{T}$	total stress tensor
N_1	first normal-stress-difference
N_2	second normal-stress-difference
λ_M	relaxation time
a	slip-parameter in Johnson-Segalman
$\dot{\gamma}_H$	shear rate in the high-shear band
$\dot{\gamma}_l$	shear rate in the low-shear band
ϵ	rescaled gap width
l	rescaled diffusive length

Appendix A

1D Adimensional DJS equations in Taylor-Couette rheometry

rr

$$\tau_{rr} + Wi(1-a)(v^{\theta\prime} - \frac{v^\theta}{r})\tau_{r\theta} = l^2[\tau''_{rr} + \frac{\tau'_{rr}}{r} + \frac{2}{r^2}(-\tau_{rr} + \tau_{\theta\theta})]$$

$r\theta$

$$\tau_{r\theta} + Wi(v^{\theta\prime} - \frac{v^\theta}{r})[-\frac{1+a}{2}\tau_{rr} + \frac{1-a}{2}\tau_{\theta\theta}] = (v^{\theta\prime} - \frac{v^\theta}{r}) + l^2[\tau''_{r\theta} + \frac{\tau'_{r\theta}}{r} - \frac{4}{r^2}\tau_{r\theta}]$$

$\theta\theta$

$$\tau_{\theta\theta} + Wi(1+a)(\frac{v^\theta}{r} - v^{\theta\prime})\tau_{r\theta} = l^2[\tau''_{\theta\theta} + \frac{\tau'_{\theta\theta}}{r} + \frac{2}{r^2}(\tau_{rr} - \tau_{\theta\theta})]$$

where $Wi \equiv \frac{\lambda_M \Omega}{\epsilon(2+\epsilon)}$, $\epsilon \equiv \frac{d}{R_1}$ and $l \equiv \sqrt{\frac{\mathcal{D}}{R_1^2}}$

θ

$$0 = \tau'_{r\theta} + \frac{2}{r}\tau_{r\theta} + \frac{\eta_S}{\eta_P}[v^{\theta\prime\prime} + \frac{v^{\theta\prime}}{r} - \frac{v^\theta}{r^2}]$$

Appendix B

3-D DJS equations in Taylor-Couette rheometry

rr

$$T_{rr} + \lambda_M[(\frac{\partial T}{\partial t})_{rr} + (v\cdot\nabla)T_{rr} - 2\frac{v^\theta}{r}T_{r\theta} - (1+a)[(T_r\cdot\nabla)v^r - \frac{v^\theta}{r}T_{r\theta}] + (1-a)\frac{\partial v^l}{\partial r}T_{lr}]$$
$$= 2\eta_p\frac{\partial v^r}{\partial r} + \mathcal{D}[\Delta T_{rr} - \frac{4}{r^2}\frac{\partial T_{r\theta}}{\partial\theta} + \frac{1}{r}\frac{\partial T_{rr}}{\partial r} + \frac{2}{r^2}(T_{\theta\theta} - T_{rr})]$$

$r\theta$

$$T_{r\theta} + \lambda_M[(\tfrac{\partial T}{\partial t})_{r\theta} + (v\cdot\nabla)T_{r\theta}$$
$$+ \tfrac{v^\theta}{r}(T_{rr} - T_{\theta\theta}) - \tfrac{1+a}{2}[(T_r\cdot\nabla)v^\theta + \tfrac{v^r}{r}T_{r\theta} + (T_\theta\cdot\nabla)v^r - \tfrac{v^\theta}{r}T_{\theta\theta}] + \tfrac{1-a}{2}(\tfrac{\partial v^l}{\partial r}T_{l\theta} + \tfrac{1}{r}\tfrac{\partial v^l}{\partial\theta}T_{lr} - \tfrac{v^\theta}{r}T_{rr} + \tfrac{v^r}{r}T_{\theta r})]$$
$$= \eta_p(\tfrac{\partial v^\theta}{\partial r} + \tfrac{1}{r}\tfrac{\partial v^r}{\partial\theta} - \tfrac{1}{r}v^\theta) + \mathcal{D}[\Delta T_{r\theta} + \tfrac{1}{r}\tfrac{\partial T_{r\theta}}{\partial r} - \tfrac{4}{r^2}T_{r\theta} + \tfrac{2}{r^2}\tfrac{\partial T_{rr}}{\partial\theta} - \tfrac{2}{r^2}\tfrac{\partial T_{\theta\theta}}{\partial\theta}]$$

rz

$$T_{rz} + \lambda_M[(\frac{\partial T}{\partial t})_{rz} + (v\cdot\nabla)T_{rz} - \frac{v^\theta}{r}T_{\theta z} - \frac{1+a}{2}[(T_r\cdot\nabla)v^z + (T_z\cdot\nabla)v^r - \frac{v^\theta}{r}T_{\theta z}] + \frac{1-a}{2}(\frac{\partial v^l}{\partial r}T_{lz} + \frac{\partial v^l}{\partial z}T_{lr})]$$
$$= \eta_p(\frac{\partial v^z}{\partial r} + \frac{\partial v^r}{\partial z}) + \mathcal{D}[\Delta T_{rz} - \frac{2}{r^2}\frac{\partial T_{\theta z}}{\partial\theta} + \frac{1}{r}\frac{\partial T_{rz}}{\partial r} - \frac{1}{r^2}T_{rz}]$$

$\theta\theta$

$$T_{\theta\theta} + \lambda_M[(\frac{\partial T}{\partial t})_{\theta\theta} + (v\cdot\nabla)T_{\theta\theta} + 2\frac{v^\theta}{r}T_{r\theta} - (1+a)[(T_\theta\cdot\nabla)v^\theta + \frac{v^r}{r}T_{\theta\theta}] + (1-a)(\frac{1}{r}\frac{\partial v^l}{\partial\theta}T_{l\theta} - \frac{v^\theta}{r}T_{r\theta} + \frac{v^r}{r}T_{\theta\theta})]$$
$$= 2\eta_p(\frac{1}{r}\frac{\partial v^\theta}{\partial\theta} + \frac{v^r}{r}) + \mathcal{D}[\Delta T_{\theta\theta} + \frac{4}{r^2}\frac{\partial T_{r\theta}}{\partial\theta} + \frac{1}{r}\frac{\partial T_{\theta\theta}}{\partial r} + \frac{2}{r^2}(T_{rr} - T_{\theta\theta})]$$

$\boxed{\theta z}$

$T_{\theta z} + \lambda_M[(\frac{\partial T}{\partial t})_{\theta z} + (v\cdot\nabla)T_{\theta z}$
$+ \frac{v^\theta}{r}T_{rz} - \frac{1+a}{2}[(T_\theta\cdot\nabla)v^z + (T_z\cdot\nabla)v^\theta + \frac{v^r}{r}T_{\theta z}] + \frac{1-a}{2}(\frac{1}{r}\frac{\partial v^l}{\partial\theta}T_{lz} + \frac{\partial v^l}{\partial z}T_{l\theta} - \frac{v^\theta}{r}T_{rz} + \frac{v^r}{r}T_{\theta z})]$
$= \eta_p(\frac{1}{r}\frac{\partial v^z}{\partial\theta} + \frac{\partial v^\theta}{\partial z}) + \mathcal{D}[\Delta T_{\theta z} + \frac{2}{r^2}\frac{\partial T_{rz}}{\partial\theta} + \frac{1}{r}\frac{\partial T_{\theta z}}{\partial r} - \frac{1}{r^2}T_{\theta z}]$

$\boxed{zz}$

$$T_{zz} + \lambda_M[(\frac{\partial T}{\partial t})_{zz} + (v\cdot\nabla)T_{zz} - (1+a)[(T_z\cdot\nabla)v^z] + (1-a)\frac{\partial v^l}{\partial z}T_{lz}] = 2\eta_p\frac{\partial v^z}{\partial z} + \mathcal{D}[\Delta T_{zz} + \frac{1}{r}\frac{\partial T_{zz}}{\partial r}]$$

NAVIER-STOKES EQUATIONS

$\boxed{r}$

$$\rho[\frac{\partial v^r}{\partial t} + (v\cdot\nabla)v^r - \frac{(v^\theta)^2}{r}] = \frac{\partial T_{rr}}{\partial r} + \frac{T_{rr}}{r} + \frac{1}{r}\frac{\partial T_{r\theta}}{\partial\theta} - \frac{T_{\theta\theta}}{r} + \frac{\partial T_{rz}}{\partial z} + \mu[\frac{\partial^2 v^r}{\partial r^2} + \frac{1}{r}\frac{\partial v^r}{\partial r} - \frac{v^r}{r^2} + \frac{1}{r^2}\frac{\partial^2 v^r}{\partial\theta^2} - \frac{2}{r^2}\frac{\partial v^\theta}{\partial\theta} + \frac{\partial^2 v^r}{\partial z^2}] - \frac{\partial p}{\partial r}$$

$\boxed{\theta}$

$$\rho[\frac{\partial v^\theta}{\partial t} + (v\cdot\nabla)v^\theta + \frac{v^r v^\theta}{r}] = \frac{1}{r}\frac{\partial T_{\theta\theta}}{\partial\theta} + \frac{\partial T_{r\theta}}{\partial r} + \frac{2}{r}T_{r\theta} + \frac{\partial T_{\theta z}}{\partial z} + \mu[\frac{\partial^2 v^\theta}{\partial r^2} + \frac{1}{r}\frac{\partial v^\theta}{\partial r} - \frac{v^\theta}{r^2} + \frac{1}{r^2}\frac{\partial^2 v^\theta}{\partial\theta^2} + \frac{2}{r^2}\frac{\partial v^r}{\partial\theta} + \frac{\partial^2 v^\theta}{\partial z^2}] - \frac{1}{r}\frac{\partial p}{\partial\theta}$$

$\boxed{r}$

$$\rho[\frac{\partial v^z}{\partial t} + (v\cdot\nabla)v^z] = \frac{T_{rz}}{r} + \frac{\partial T_{rz}}{\partial r} + \frac{1}{r}\frac{\partial T_{\theta z}}{\partial\theta} + \frac{\partial T_{zz}}{\partial z} + \mu[\frac{\partial^2 v^z}{\partial r^2} + \frac{1}{r}\frac{\partial v^z}{\partial r} + \frac{1}{r^2}\frac{\partial^2 v^z}{\partial\theta^2} + \frac{\partial^2 v^z}{\partial z^2}] - \frac{\partial p}{\partial z}$$

INCOMPRESSIBILITY $\quad \frac{\partial v^r}{\partial r} + \frac{v^r}{r} + \frac{1}{r}\frac{\partial v^\theta}{\partial\theta} + \frac{\partial v^z}{\partial z} = 0$

where the following notations have been used: $(T_i\cdot\nabla)f \equiv T_{ir}\frac{\partial f}{\partial r} + T_{i\theta}\frac{1}{r}\frac{\partial f}{\partial\theta} + T_{iz}\frac{\partial f}{\partial z}$ and $\frac{\partial v^l}{\partial r}T_{lr} \equiv \frac{\partial v^r}{\partial r}T_{rr} + \frac{\partial v^\theta}{\partial r}T_{\theta r} + \frac{\partial v^z}{\partial r}T_{zr}$

Appendix C

Matrix A of the linear stability analysis

Rows of matrix **A**(m,k) correspond to the projection of the equations on the component indicated in the first column of the table below. Columns are the prefactors of the perturbative component indicated in the first line. The following terms have to be added to the diagonal of the matrix : $Diagonal_1$ for rows between 1 and 6, $Diagonal_2$ for rows between 7 and 9.

$$Diagonal_1 = -1 - Wi\, v^{\theta}{}^{im}/_r + \mathcal{I}^2(\partial_r^2 - {}^{m^2}/_{r^2} + k^2 + \frac{\partial_r}{r})$$

$$Diagonal_2 = -\rho v^{\theta}{}^{im}/_r + {}^{\eta_s}/_{\eta_p}(\partial_r^2 + \frac{\partial_r}{r} - {}^{m^2}/_{r^2} + k^2)$$

	T_{rr}	$T_{r\theta}$	T_{rz}	$T_{\theta\theta}$	$T_{\theta z}$	T_{zz}	v^r	v^θ	v^z	$\boldsymbol{p}$
rr	$-2{}^{\mathcal{I}^2}/_{r^2}$	$Wi(1-a)({}^{v^\theta}/_r - v^{\theta\prime}) - 4\mathcal{I}^2{}^{im}/_{r^2}$		$2{}^{\mathcal{I}^2}/_{r^2}$			$Wi[-\partial_r T^\star_{rr} + 2aT^\star_{rr}\partial_r + (1+a)T^\star_{r\theta}{}^{im}/_r] + 2\partial_r$	$Wi(1-a)T^\star_{r\theta}({}^1/_r - \partial_r)$		
$r\theta$	$Wi\frac{1+a}{2}(v^{\theta\prime} - {}^{v^\theta}/_r) + 2\mathcal{I}^2{}^{im}/_{r^2}$	$-4{}^{\mathcal{I}^2}/_{r^2}$		$Wi\frac{1-a}{2}({}^{v^\theta}/_r - v^{\theta\prime}) - 2\mathcal{I}^2{}^{im}/_{r^2}$			$Wi\,[aT^\star_{r\theta}({}^1/_r + \partial_r) - \partial_r T^\star_{r\theta} + (\frac{1+a}{2}T^\star_{\theta\theta} - \frac{1-a}{2}T^\star_{rr})^{im}/_r] + {}^{im}/_r$	$Wi\,[(\frac{1+a}{2}T^\star_{rr} - \frac{1-a}{2}T^\star_{\theta\theta})(\partial_r - {}^1/_r) + aT^\star_{r\theta}{}^{im}/_r] + (\partial_r - {}^1/_r)$		
rz			$-{}^{\mathcal{I}^2}/_{r^2}$		$Wi\frac{1-a}{2}({}^{v^\theta}/_r - v^{\theta\prime}) - 2\mathcal{I}^2{}^{im}/_{r^2}$		$k - Wi\frac{1-a}{2}T^\star_{rr}k$	$-Wi\frac{1-a}{2}T^\star_{r\theta}k$	$Wi\frac{1+a}{2}(T^\star_{rr}\partial_r + T^\star_{r\theta}{}^{im}/_r) + \partial_r$	

	T_{rr}	$T_{r\theta}$	T_{rz}	$T_{\theta\theta}$	$T_{\theta z}$	T_{zz}	v^r	v^θ	v^z	$\boldsymbol{p}$
$\theta\theta$	$2\mathcal{I}^2/r^2$	$Wi(1+a)(v^{\theta\prime}-v^\theta/r)+4\mathcal{I}^2 im/r^2$		$-2\mathcal{I}^2/r^2$			$Wi\,[2a\frac{T^\star_{\theta\theta}}{r}-\partial_r T^\star_{\theta\theta}-(1-a)T^\star_{r\theta}\,im/r]+2/r$	$Wi\,(1+a)T^\star_{r\theta}(\partial_r-1/r)+2aT^\star_{\theta\theta}\,im/r]+2im/r$		
θz			$Wi\frac{1+a}{2}(v^{\theta\prime}-v^\theta/r)+2\mathcal{I}^2 im/r^2$		$-\mathcal{I}^2/r^2$		$-Wi\frac{1-a}{2}T^\star_{r\theta}k$	$-Wi\frac{1-a}{2}T^\star_{\theta\theta}k+k$	$im/r+Wi\frac{1+a}{2}(T^\star_{\theta\theta}\,im/r+T^\star_{r\theta}\partial_r)$	
zz									$2k$	
r	$(1/r+\partial_r)$	im/r	k	$-1/r$			$-\eta_s/\eta_p\,1/r^2$	$2\rho v^\theta/r-2\eta_s/\eta_p\,im/r^2$		$-\partial_r$
θ		$(2/r+\partial_r)$		im/r	k		$-\rho(v^{\theta\prime}+v^\theta/r)+2\eta_s/\eta_p\,im/r^2$	$-\eta_s/\eta_p\,1/r^2$		$-im/r$
z			$(1/r+\partial_r)$		im/r	k				$-k$
$inc.$							$(1/r+\partial_r)$	im/r	k	

Appendix D

Interfacial Boundary conditions for the Taylor-Couette Split Fluid

The impermeability condition at the interface reads:

$$v'^{I} \cdot \underline{n} = v'^{II} \cdot \underline{n} = V \cdot \underline{n} \tag{D.0.1}$$

which turns into, at first order:

$$-v_\theta^I \partial_\theta h + \delta v_r^I = \frac{\partial h}{\partial t} \quad \text{and} \quad \delta v_r^I = \delta v_r^{II}$$

The continuity of the tangential velocities reads (when neglecting higher order terms): $\Delta[\delta v_\theta + D_r v_\theta \cdot h] = 0$ and $\delta v_z^I = \delta v_z^{II}$

- ⋆ Stress

$$\Delta[\underline{\underline{\Sigma}} \cdot \underline{n}] = \Gamma \kappa \underline{n}$$

Projecting on x, given that $[D_\theta \Sigma_{r\theta}] = 0$ in each phase, $\Delta\delta\Sigma_{r\theta} - \partial_\theta h \cdot \Delta\Sigma_{\theta\theta} = 0$

$$\Delta[\delta T_{r\theta} + \eta_s(\partial_\theta \delta v_r + \partial_r \delta v_\theta) + \partial_\theta h \cdot (p - T_{\theta\theta})] = 0$$

Projecting on y: $\partial_\theta h \cdot \Delta\Sigma_{r\theta} + \Delta\delta\Sigma_{rr} = (\frac{1}{r_0^2}\frac{\partial^2 h}{\partial\theta^2} + \frac{\partial^2 h}{\partial z^2})\Gamma$

$$0 + \Delta[\delta T_{rr} + 2\,\eta_s \partial_r \delta v_r - \delta p] = -(\frac{1}{r_0^2}\frac{\partial^2 h}{\partial\theta^2} + \frac{\partial^2 h}{\partial z^2})\Gamma$$

Projecting on z: $\partial_z h \cdot \Delta p + \Delta\delta\Sigma_{rz} = 0$

$$\partial_z h \cdot \Delta p + \Delta[\delta T_{rz} + \eta_s(\partial_r \delta v_z + \partial_z \delta v_r] = 0$$

Bibliography

[1] P. Debye & E.W. Anacker, Micelle shape from dissymmetry measurements, *J. Phys. Chem.*, Vol.55, 644-655, 1951 1.1.1

[2] S. Lerouge & J.F. Berret, Shear-induced transitions and instabilities in surfactant wormlike micelles, *Adv. Polym. Sci.*, Springer Berlin/Heidelberg, 2009 1, 2.2.1

[3] S. Lerouge, M.A. Fardin, M. Argentina, G. Grégoire & O. Cardoso, Interface dynamics in shear-banding flow of giant micelles, *Soft Matter*, 2008 2.4.1, 4.6, 1, 6.3.2

[4] M.A. Fardin, B. Lasne, O. Cardoso, G. Grégoire, M. Argentina, J.P. Decruppe & S. Lerouge, Taylor-like Vortices in Shear-Banding Flow of Giant Micelles, *Phys. Rev. Letters*, Vol. 103, 028302, 2009 (document), 3

[5] J-F Berret, Rheology of wormlike micelles: Equilibrium properties and shear-banding transition, *Molecular Gels*, Part 6, 667-720, 2006 1, 1.1.1, 1.1.2, 1, 1.2.5, 2.2.1

[6] H. Rehage & H. Hoffmann, Viscoelastic surfactant solutions: model systems for rheological research, *Molecular Physics*, Vol.74, No. 5, 933-973, 1991 1, 1.1.1, 1.1.2

[7] M.E. Cates & S.M. Fielding, Rheology of Giant Micelles, *Advances in Physics*, Vol.55, No 7-8, 799-879, 2006 (document), 1, 1.1.2, 1.2.4, 3, 1.3, 1.3.3

[8] D. Quéré, Surfaces Molles, Éditions de l'École Polytechnique, 2006, Chapters 7 and 9, 2007 1, 1.2.1

[9] J. Israelashvili, *Intermolecular and surface forces*, Academic Press, 1985 1, 1.2.3

[10] R.G. Larson, *The structure and Rheology of Complex Fluids*, Oxford University Press, 1999 1, 1.1.1, 1.2.4, 1.2.5, 1.3.3

[11] E. Cappelaere & R. Cressely, Shear-banding structure in viscoelastic micellar solutions, *Colloid Polymer Sci*, 275, 407-418, 1997 1, 1.2.5

[12] M.E. Cates, Reptation of Living Polymers: Dynamics of Entangled Polymers in the Presence of Reversible Chain-Scission Reactions, *Macromolecules*, Vol.20, No. 9, 1987 1.3.3, 1.3.3

[13] P.-G. de Gennes, Reptation of a polymer chain in the presence of fixed obstacles, *J. Chem. Phys.*, Vol.55, 1971 1.3.3

[14] L. Bécu, D. Anache, S. Manneville & A. Colin, Evidence for three-dimensional unstable flows in shear-banding wormlike micelles, *Phys. Rev. E*, Vol.76, 011503, 2007 (document), 2.2.1, 2.4.4, 3, 4.1.1

[15] R.W. Mair & P.T. Callaghan, Observation of shear-banding in worm-like micelles by NMR velocity imaging, *Europhys. Letters*, Vol.36, No. 9, 719-724, 1996 2.2.1

[16] M.M. Britton & P.T. Callaghan, Nuclear magnetic resonance visualization of anomalous flow in cone-and-plate rheometry, *J. Rheol.*, Vol.41, No.6, 1997 6.2.2

[17] P.D. OlMsted, O. Radulescu & C.-Y.D. Lu, Johnson-Segalman model with a diffusion term in cylindrical Couette-flow, *J. Rheol.*, Vol.44, No.2, 2000 5

[18] O. Radulescu, P. D. Olmsted & C.-Y.D. Lu, Shear banding in reaction-diffusion models, *Rheol. Acta*, Vol.38, 606-613, 1999 2.3.2, 6

[19] A.W. El-Kareh & L.G. Leal, Existence of Solutions for all Deborah Numbers for a Non-Newtonian Model Modified to Include Diffusion, *J. Non-Newt. Fluid. Mech.*, Vol.33, 257-257, 1989 2.3.1

[20] S.M. Fielding, Viscoelastic Taylor-Couette Instability of Shear Banded Flow, *Phys. Rev. Letters*, Vol.104, 198303, 2010 3.1, 3.1.2, 3.2, 4.1, 4.1.1, 4.2.2

[21] S.M. Fielding, Complex dynamics of shear banded flows, *Soft Matter*, Vol.3, 1262-1279, 2007 3.2

[22] P. Pakdel & G.H. McKinley, Elastic Instability & Curved Streamlines, *Phys. Rev. Letters*, Vol. 77, No 12, 1996 4.1.2

[23] A.N. Morozov & W. van SAARLOOS, An introductory essay on subcritical instabilities and the transition to turbulence in visco-elastic parallel shear flows, *Phys. Reports*, Vol.447, No. 3-6, 112-143, 2007 4.1.2

[24] R.G. Larson, E.S.G. Shaqfeh & S.J. Muller, A purely elastic instability in Taylor-Couette flow, *J. Fluid. Mech.*, Vol.218, 573-600, 1990 4.1.2

[25] S. Kumar & R.G. Larson, Shear banding and secondary flow in viscoelastic fluids between a cone and plate, *J. Non-Newtonian Fluid Mech.*, Vol.95, 295-314, 2000

4.2.1, 6.2.2